npj | materials degradation

Published in partnership with CSCP and USTB

Article

https://doi.org/10.1038/s41529-026-00811-x

Effect of volume fractions and aging on Ni-GDC SOFC anode degradation and performance: multiphase-field simulations

Ravi Kumar Jeela[1,2] ✉, **Ahmed Elmoghazy**[2], **Lukas Schöller**[2], **Matthias Wieler**[3], **Andreas Prahs**[2,4], **Daniel Schneider**[1,2,4] ✉ & **Britta Nestler**[1,2,4]

Enhancing the performance and durability of solid oxide fuel cells (SOFCs) requires concurrent improvements in electrochemical activity and mechanical integrity, both strongly dependent on the initial anode microstructure and its degradation over long-term operation. This study presents a comprehensive degradation investigation for nickel-gadolinium doped ceria (Ni-GDC) SOFC anode microstructures, combining the generation of realistic synthetic microstructures and large-scale aging simulations. Synthetic microstructures are generated and quantitatively validated against experimental reconstructions of Ni-GDC employing an enhanced structure generator workflow that incorporates sintering-like morphological coalescence, resulting in digital twins for optimization studies. Representative synthetic microstructures are generated with systematically varying phase volume fractions and subjected to long-term (2000 h) aging using a validated multiphase-field model. Electrochemical performance descriptors, including triple-phase boundary (TPB), double-phase boundary (DPB) densities, phase tortuosities, and mechanical properties, such as elastic moduli and stress distributions resulting from thermal expansion coefficient mismatch between Ni and GDC, are collectively analyzed. The results provide detailed insights into the design of anode microstructures by highlighting trade-offs between initial and degradation-induced electrochemical and mechanical performance.

Solid oxide fuel cells (SOFCs), characterized by fuel flexibility and high operating temperatures (600 °C−900 °C), are promising energy conversion devices. Improving their cost-effectiveness and long-term reliability requires design strategies incorporating both micro- and macrostructural effects influencing electrochemical performance and stability[1]. Although yttrium-stabilized zirconia (YSZ) is typically the electrolyte and anode support material, gadolinium-doped ceria (GDC) is emerging as a promising alternative due to its superior ionic conductivity even at lower temperatures of 500 °C [2,3]. In reducing atmospheres, GDC exhibits mixed ionic-electronic conductivity (MIEC)[4], thereby enabling electrochemical reactions to occur not only at triple-phase boundaries (TPBs), defined as the line or region where the electron conductor, ion conductor, and gas phase intersect, as in Ni-YSZ anodes, but also at extended sites of double-phase boundaries (DPBs) between pores and MIEC materials, improving electrochemical performance. Thus, the application of doped ceria can allow extension of the operating range of SOFCs to lower temperatures, referred to as intermediate temperature SOFCs (IT-SOFCs). Despite these advantages, performance degradation during long-term operation remains a critical challenge limiting the commercialization of SOFCs.

A major contributor to the degradation of the SOFC anode is the morphological evolution of the 3D porous electrode microstructure during operation. In Ni-based anodes, degradation is primarily caused by Ni coarsening, agglomeration, and depletion[5–7]. While the zirconia matrix in Ni-YSZ anodes is relatively stable, Ni-GDC anodes exhibit notable GDC

---

[1]Institute of Digital Materials Science (IDM), Karlsruhe University of Applied Sciences, Karlsruhe, Germany. [2]Institute for Applied Materials - Microstructure Modelling and Simulation (IAM-MMS), Karlsruhe Institute of Technology (KIT), Karlsruhe, Germany. [3]Computational Materials Engineering (CR/ATC1), Robert Bosch GmbH, Renningen, Germany. [4]Institute of Nanotechnology - Microstructure Simulations (INT-MSS), Karlsruhe Institute of Technology (KIT), Eggenstein-Leopoldshafen, Germany. ✉e-mail: ravi_kumar.jeela@h-ka.de; daniel.schneider@kit.edu

phase evolution, resulting in more complex microstructural dynamics[5,8]. Several experimental studies reported their findings under electrochemical operating conditions, whereas some were conducted under purely thermal open circuit voltage (OCV) conditions[8,9]. Recently, under humidified thermal OCV conditions, Liu et al.[9] reported Ni coarsening along with minor GDC growth, without any evidence of nano-GDC particles or nanoscale changes in the GDC phase. Understanding the degradation of solid oxide cells (SOC) resulting from microstructural evolution is essential for predicting long-term cell performance and durability. In this regard, microstructural simulations can play an integral role in understanding SOC degradation by reducing time and cost, and complementing experiments. However, their predictive capability is strongly determined by the identification of a suitable model for coarsening in Ni-GDC anodes, along with accurately calibrated parameters for Ni-GDC systems.

The phase-field method[10–13] is used in conjunction with SOFC anodes to investigate microstructural evolutions[14–19]. In this regard, the multiphase-field (MPF) model based on grand-potential formulation[20,21] presents a few advantages, including independent control of binary interfacial energies, uniform and finite interfacial thicknesses, and quantitative representation of interfacial diffusion, enabling the direct incorporation of experimentally measured surface diffusion coefficients and contact angles. It is noteworthy to mention that the above-mentioned phase-field studies were primarily focused on Ni-YSZ anodes, where microstructural evolution is dominated by Ni coarsening, while the YSZ phase remains largely stable. In contrast, phase-field investigations of Ni-GDC systems remain relatively unexplored due to their complexity, as the evolution of both the Ni and GDC phases results in a more complex microstructural evolution. Sun et al.[22] developed an integrated mesoscale model to predict long-term morphological and performance-related degradation in Ni-GDC anodes. Previous work, while informative, relied on indirect validation and was limited to three literature-based descriptors, i.e., the mean particle diameters of Ni, GDC, and the TPB density. Recently, Chang et al.[23] developed a multi-scale simulation framework combining discrete element modeling to generate initial Ni-GDC anode microstructures and a phased-field model to simulate the evolution of the Ni-GDC anode microstructure. In their work, validation of the generated microstructures was limited to a small set of descriptors, primarily TPB density and tortuosities of GDC and pore, and the simulation results were validated against experiments using primarily TPB density values from the literature. Due to computational limitations, the modeled electrode volume was restricted to 3.5 μm x 3.5 μm x 1.1 μm, limiting the representativeness of the anode microstructure.

In our previous work[24], we performed quantitative 3D phase-field simulations of Ni and GDC coarsening in Ni-GDC SOFC anodes, using experimentally reconstructed pristine microstructures and quantitative validation using aged microstructures (240 h and 1100 h) across an extensive set of metrics. Due to the scarcity of literature data for Ni-GDC systems, the required interface and diffusion parameters were determined using a Bayesian active learning framework[25]. In the current work, this validated model is employed to perform large-scale aging simulations over a systematically generated set of initial synthetic microstructures. This work utilizes the Phase-field Algorithms for Computational Engineering in 3D (PACE3D) simulation framework[26], a powerful multi-physics environment enabling physics-based predictive modeling of microstructural evolution driven by a range of influencing mechanisms[27]. Its highly efficient vectorized SIMD (Single-Instruction Multiple-Data) solver, described in detail in the work of Seiz et al.[28], constitutes the computational core for aging simulations.

It is well established that SOFC anode microstructures profoundly influence macroscopic properties, including mechanical integrity and electrochemical performance. In particular, porosity has been shown to influence the elastic modulus and biaxial strength significantly[29–31]. Despite extensive studies on electrochemical behavior and microstructure evolution, direct and time-resolved investigations of mechanical property degradation under steady-state, isothermal aging conditions remain scarce. These studies are critical since the anode serves as a load-bearing component in many SOFC designs, such as anode-supported and metal-supported cells, where microstructural changes directly affect mechanical reliability[32]. Liu et al.[33] developed a deep learning-based homogenization framework that links porous Ni-YSZ anode microstructures to effective macroscopic properties, including elastic modulus, Poisson's ratio, shear modulus, and thermal expansion, and demonstrates their dependence on porosity and Ni content. However, their work was limited to Ni-YSZ anodes, and the effects of aging, as well as the influence of electrolyte volume fraction, were not investigated. More recently, Elmoghazy et al.[34] performed strain-controlled numerical homogenization to evaluate the evolution of effective elastic properties in Ni-GDC anodes during aging, but their analysis was confined to a single initial microstructural configuration. Thus, a systematic investigation of how variations in initial Ni-GDC microstructures, particularly phase volume fractions, affect effective mechanical properties and their degradation during aging is still lacking. To the best of our knowledge, this has not been comprehensively addressed in the literature. In multi-scale and multi-physics SOFC modeling, accurate macroscopic mechanical parameters are essential for stress analysis under thermal loading[35]. Since these properties are determined by the microstructure of the electrode, establishing quantitative correlations between microstructural features and macroscopic mechanical responses, together with electrochemically relevant metrics such as TPBs, DPBs, and tortuosities, is essential.

The electrochemical performance of Ni-GDC SOFC anodes strongly depends on microstructural properties such as TPB and DPB densities, defining the available sites for electrochemical reactions, as well as the tortuosity of the Ni, GDC, and pore phases, controlling the electron, ion, and gas transport through the porous network. The initial phase volume fractions and particle sizes of the microstructure strongly influence these properties, enabling microstructure optimization through tailored electrode compositions and particle sizes to enhance performance. In experimental optimization studies, however, the number of microstructures being investigated is inherently limited, as the fabrication of Ni-GDC samples, 3D microstructure characterization using advanced imaging techniques such as Focused Ion Beam Scanning Electron Microscopy (FIB-SEM), and the large-scale aging studies to assess degradation are time-consuming, resource-intensive, and costly. As an alternative, numerical modeling approaches have been widely used to overcome these limitations, as they enable the rapid generation and systematic evaluation of a large number of microstructures[36–38]. Despite advances in modeling synthetic microstructures, accurately reproducing the complex microstructures of SOFC anodes, formed by the sintering of multi-component particles, remains a challenge. Sintering-induced particle overlap was implemented by simply enlarging the particle sizes[39]. A similar dilatation-based method was also employed by Zheng et al.[40] to reproduce sintering effects. Furthermore, key geometric and statistical descriptors, such as phase volume fractions and particle size distributions, are not always controllable in modeling approaches. Since the systematic optimization of the microstructure is based on these descriptors, the possibility to control these is crucial during the creation of structures in generator models. In this work, we extend and adapt a flexible virtual structure generator originally developed by Schöller et al.[41] for multi-layer SOFC microstructures. The underlying framework of their work builds upon methods developed by Feinauer et al.[42] and Westhoff et al.[37] for modeling lithium batteries and has been tailored to the specific requirements of multilayer SOFC architectures.

The microstructures of SOFC electrodes are defined by several independent parameters, such as phase volume fractions and particle sizes, which influence both initial performance and long-term degradation. Optimizing for the slowest degradation may not necessarily result in optimal initial performance, highlighting the complexity of microstructure design. Timurkutluk et al.[43] systematically examined TPB density as a function of particle size and phase volume fractions in synthetic SOFC electrode microstructures by generating a large number of virtual microstructures and evaluating performance based solely on TPB density. Prioux et al.[44] proposed a multiscale modeling framework for optimizing Ni-YSZ hydrogen electrode microstructures, utilizing experimentally measured electrochemical data at the cell level and 3D electrode reconstructions as references, and coupling synthetic microstructures with electrochemical models on the cell and electrode levels. Mütter et al.[45] applied an artificial neural network for optimizing process parameters. Despite attempts to optimize microstructure in SOFC research, this domain is still evolving, mainly as a result of limited understanding of microstructure evolution phenomena. Peng et al.[46] highlighted this research gap in a comprehensive review study. Optimizing electrode microstructures in such a high-dimensional parameter space requires extensive modeling efforts combined with a systematic investigation of independent parameters affecting performance in pristine structures as well as over long-term operation, both of which we have presented here.

In this work, we extend an original structure generator workflow[41] to generate a realistic digital twin of Ni-GDC anode microstructures. The extended workflow introduces a computationally efficient, sintering-like morphological coalescence step based on a modified Allen-Cahn formulation with volume preservation[47] and a correction term controlling curvature minimization[48] to replicate the sintering process in experimentally fabricated anodes without explicitly simulating physical mechanisms. The digital twin is rigorously validated against FIB-SEM reconstructed 3D Ni-GDC anode microstructures by incorporating seventeen quantitative structural, geometrical, electrochemical, and mechanical relevant descriptors. Fifteen synthetic microstructures are generated systematically by varying the Ni, GDC, and pore volume fractions to investigate microstructural degradations. The aging behavior of Ni-GDC anodes is predicted using a multiphase-field model based on the grand-potential functional, previously validated against experimentally aged structures[24] and parameterized using Bayesian active learning methods[25] to simulate long-term (2000 h) coarsening under thermal operating conditions. The mechanical response of Ni-GDC anode microstructures is evaluated using a quasi-static solid mechanics formulation with strain-controlled homogenization to estimate effective elastic moduli and the stack boundary conditions method, enabling coupled evolution of stress and strain resulting from thermal expansion and mechanical confinement[34]. Electrochemical performance-relevant descriptors such as TPBs, DPBs, and phase tortuosities, as well as mechanical integrity-relevant descriptors such as elastic moduli, average von Mises stress, and critical volume fractions (CVF), are analyzed as functions of phase volume fractions in pristine structures and their temporal evolution during isothermal aging, providing comprehensive insights into the design and degradation of Ni-GDC SOFC anodes.

Results and Discussion

This section systematically investigates the influence of the volume fractions of nickel, GDC, and pore phases in synthetic microstructures on both the initial and long-term performance of Ni-GDC SOFC anodes. First, the influence on microstructural properties relevant to electrochemical performance, such as TPB and DPB densities, along with the tortuosity of the phases determining ion, electron, and gas transport, is analyzed in the pristine state, followed by the corresponding effects on effective mechanical properties and response. Subsequently, multiphase-field simulation results investigating the coarsening behavior of various synthetic microstructures under thermal operating conditions of 900 °C with a gas composition of H_2-50%/H_2O-50% are presented. The evolution of microstructure over time is examined through particle diameter analysis, after which the influence of aging on microstructural properties relevant to electrochemical performance is discussed, followed by the effective mechanical properties in the aged state.

Influence of initial microstructure on descriptors of electrochemical performance

TPBs represent the electrochemical reaction sites in both Ni-YSZ and Ni-GDC SOFC anodes. Figure 1(a) compares the influence of phase volume fractions on the total TPB density across all investigated synthetic microstructures. As expected, the TPB density shows a strong dependence on the phase volume fractions. For each porosity group, the TPB density initially increases, reaches a maximum at nearly equal Ni/GDC solid volume fractions, and then decreases thereafter. The TPB density values are highest at the equivalent Ni/GDC solid volume fraction (50/50) for the structures, except for the group with 45% porosity. Furthermore, the TPB densities for Ni/GDC compositions of 50/50 and 60/40 show only minimal differences. Overall, the maximum TPB densities among the groups are observed for structures A3, B3, and C4, which reach 4.98, 4.04, and 3.22 μm^{-2}, respectively. The highest TPB density can be seen in a group with 25% porosity, as expected from the higher volume fractions of nickel and GDC. These results are consistent with the percolation-based analyses reported in the literature[49–51]. With comparable particle radii of the two solid phases, the TPB density increases with the solid phase fraction, reaches a maximum at the equivalent phase composition, followed by a decrease. In the current work, the highest TPB density occurs in the A3 configuration, where nickel and GDC represent around 37.5 vol.% respectively, and the pore is 25 vol.%.

DPBs also contribute to the electrochemical activity in Ni-GDC SOFC anodes due to the mixed ionic and electronic conductivity of GDC, making the GDC/Pore interface an additional site to the TPBs as electrochemical reaction sites. As depicted in Fig. 1b, the DPB density decreases with decreasing GDC solid volume fraction for all porosity groups A, B, C from 1.80–2.02 to 0.86–0.96 μm^{-1}. Within each group, a higher GDC content (solid volume fraction) leads to an increased DPB density as a result of the increased available GDC surface area. Across different porosities (A, B, C groups), however, a distinctive trend can be observed: Structures with a porosity of 25% consistently exhibit lower DPB densities, while those with a porosity of 35% and 45% exhibit higher and nearly identical values, suggesting saturation. This behavior emphasizes that DPB density depends on both the GDC volume fraction and the pore phase, as well as connectivity. At lower porosity (25%), the pore phase is poorly percolated, as reflected in high pore tortuosity values (in the range of 5.5–10; Fig. 1e), limiting contact between GDC, pores, and rendering a significant fraction of the GDC surface confined within the solid network. Increasing the porosity to 35% significantly improves pore connectivity (tortuosity in the range of 2.7-3.4; Fig. 1e), uncovering more GDC surface area and increasing the DPB density. A further increase in porosity to 45% leads to no further enhancement in DPB density, indicating a saturation stage in which nearly all accessible GDC surfaces are already in contact with the pore phase. Overall, systems with a porosity of 35% (group B) deliver better results with regard to DPB densities.

TPB and DPB densities are not the sole determining factors for the electrochemical performance of Ni-GDC SOFC anodes; the efficient transport of fuel gas, electrons, and oxide ions is equally essential. The transport of gas is determined by pore phase contiguity, while continuous Ni and GDC pathways enable electronic and ionic conduction. Microstructure influence on these transport processes can be quantified by tortuosity: higher values indicate poorly connected phases with long and convoluted paths that impede transport, while lower values correspond to well-connected, short, and relatively straight paths that enable efficient transport. Indefinite tortuosity values indicate a non-percolating phase for which effective transport is not possible. Figure 1c–e shows the volume-dependent tortuosity of the Ni, GDC, and pore phases, averaged over the three principal directions.

Across all porosity groups, Ni tortuosity decreases with increasing Ni volume fraction, reflecting improved phase connectivity, a general trend reported for porous multiphase systems (Fig. 1c). Structures with Ni volume fractions of 16.78% (C1), 19.67% (B1), 22.08% (C2), and 22.51% (A1) exhibit non-percolating Ni and thus infinite tortuosity, while the closest percolating case of B2 (25.71% Ni) exhibits connectivity yet with a high tortuosity value of 31.36. These trends align with the experimental Ni-GDC microstructure analyzed in this study, where a Ni volume fraction of 21.92% results in a non-percolating Ni structure, even though the mean particle size (0.91 μm) is larger than in the synthetic structures (0.75 μm), but the particle size ratios are comparable (Ni/GDC is 1.59 in the experimental structure and 1.50 in the synthetic structure). In contrast, Ni volume fractions between 37.60% and 52.71% result in well-connected pathways, with

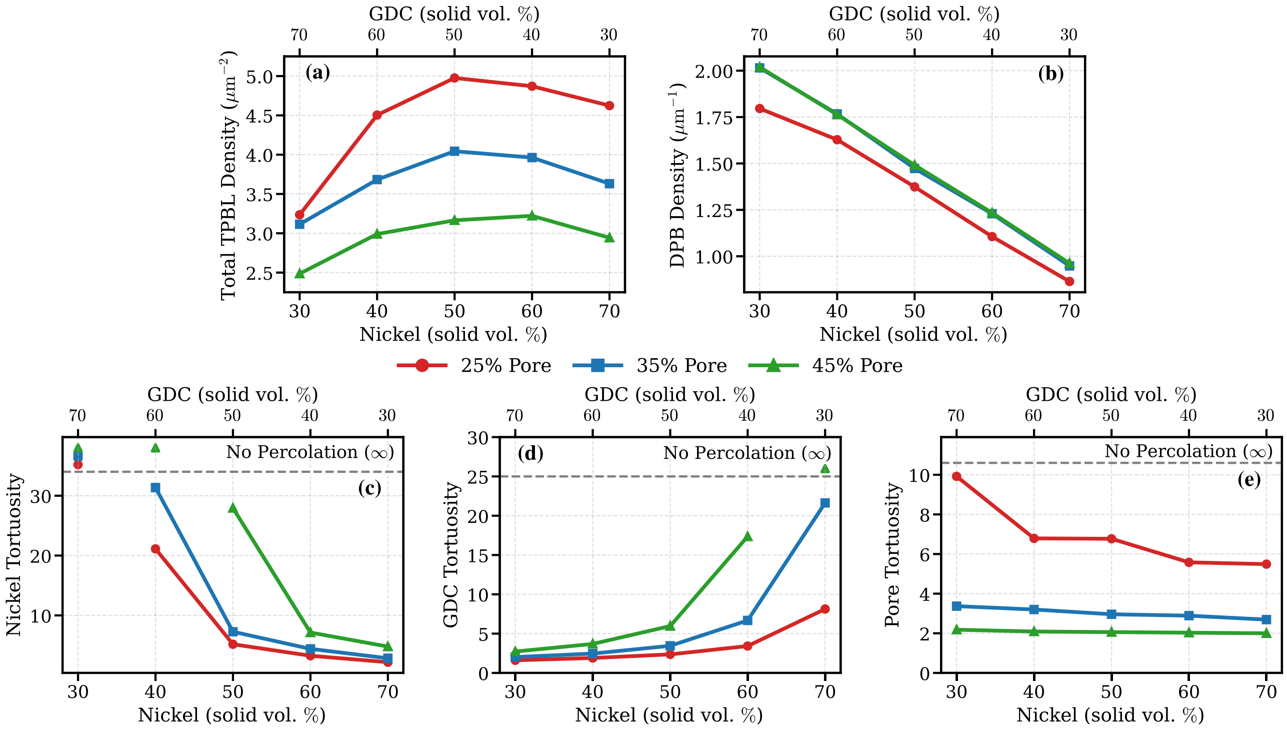

Fig. 1 | Variations in microstructural properties depending on porosity and solid volume fractions (solid vol. %) of nickel/gadolinium-doped ceria (Ni/GDC) phases. **a** total triple-phase boundary lines (TPBL) density, (**b**) double-phase boundary (DPB) density, and mean tortuosities of **c** Ni, **d** GDC, **e** pore.

tortuosity decreasing from 5.18 to 2.18. Although GDC offers mixed ionic and electronic conductivity, its electronic conductivity is several orders of magnitude lower than that of Ni[52]. Consequently, anodes with low or non-percolating Ni fraction may still be viable if GDC and pore phases are well connected, subject to design considerations, such as the thickness of the anode functional layer, and the dominant rate-limiting transport mechanism. Thus, the present results provide quantitative insight into the selection of Ni and GDC volume fractions tailored to specific cell designs, and the extracted microstructural parameters provide needed input for transmission line modeling of Ni-GDC SOFC anodes for cell performance as a function of microstructural composition.

The tortuosity of the GDC phase primarily determines the transport of oxide ions and primary or auxiliary electrons in SOFC anodes. As shown in Fig. 1d, GDC tortuosity decreases with increasing GDC volume fraction across all porosity groups, showing a similar trend to the Ni phase. However, GDC percolation is achieved at lower volume fractions: only a single structure (C5, 16.50% GDC) is non-percolating, while the closest percolating case (B5, 19.34% GDC) exhibits a connected structure, with a high tortuosity (21.63). The experimental Ni-GDC microstructure analyzed in this study, with a GDC volume fraction of 41.57%, resulted in a mean tortuosity of 2.51, whereas the synthetic structure B2 (39.13% GDC) with a tortuosity of 2.46 comes close to these results. Overall, GDC volume fractions in the range of 30.52 to 52.37% result in well-connected transport pathways, with tortuosity decreasing from 3.69 to 1.61. GDC exhibits a lower percolation threshold and a lower tortuosity compared to Ni at equivalent phase volume fractions, indicating that transport connectivity is governed not only by volume fraction and particle size, but also possibly by phase interactions and microstructural evolution during fabrication of the anode. Due to their larger size, Ni particles form fewer Ni-Ni contacts and can be disrupted more easily by surrounding GDC phases; consequently, Ni connectivity could be interrupted, leading to higher tortuosity and a higher percolation threshold. In contrast, the smaller GDC particles exhibit higher coordination and denser packing, enabling percolation at lower volume fractions and resulting in lower tortuosity. In the three-phase Ni-GDC-pore system, phase connectivity is furthermore explained by sintering-induced coalescence driven by particle size ratios, initial contact statistics, and interfacial thermodynamics. While Ni coalesces at a faster rate due to higher diffusivity and surface energy, these factors do not necessarily enhance long-distance connectivity. GDC with slower coalescence and lower surface energy instead develops smoother and more continuous networks, eventually leading to long-distance connectivity.

Pore tortuosity is another important indicator for gas transport in the anode, with higher values indicating more convoluted diffusion paths and reduced accessibility of reactants to sites of electrochemical reactions. As shown in Fig. 1e, pore tortuosity decreases with increasing porosity, as expected: Group A (25% porosity) shows the highest values, while Group C (45% porosity) shows the lowest values, reflecting improved pore connectivity. A pronounced decrease in tortuosity can be observed between 25% and 35% porosity, while small changes are observed between 35% and 45%, suggesting saturation once a well-connected pore network is established. At a fixed porosity, pore tortuosity is additionally influenced by the ratio of Ni/GDC solid volume fractions due to the differing particle sizes. Across all porosity groups, an increase in the Ni fraction resulted in lower pore tortuosity. Specifically, pore tortuosity decreases from 9.92 to 5.49 in group A, from 3.37 to 2.69 in group B, and from 2.18 to 2.00 in group C as the Ni/GDC ratio changes from 30/70 to 70/30. The influence of the solid phase composition is most prominent at low porosity (group A) and is negligible at high porosity (group C), which is consistent with the saturation of the pore network. This behavior reflects the interaction between particle size, solid volume fractions, and porosity: at constant porosity, a higher proportion of larger Ni particles tends to result in coarser pore channels, while a higher proportion of smaller GDC particles narrows the pore necks and increases the complexity of the pathways. The experimental Ni-GDC anode microstructure with a pore volume fraction of 36.51% features a mean pore tortuosity of 2.68, corresponding well with the synthetic structures in group B (35% porosity), where values range between 3.37 and 2.69 depending on the Ni/GDC ratio.

Influence of initial microstructure on effective mechanical properties

As described in detail in Microstructure quantification section, this work employs a homogenization method in which the heterogeneous anode

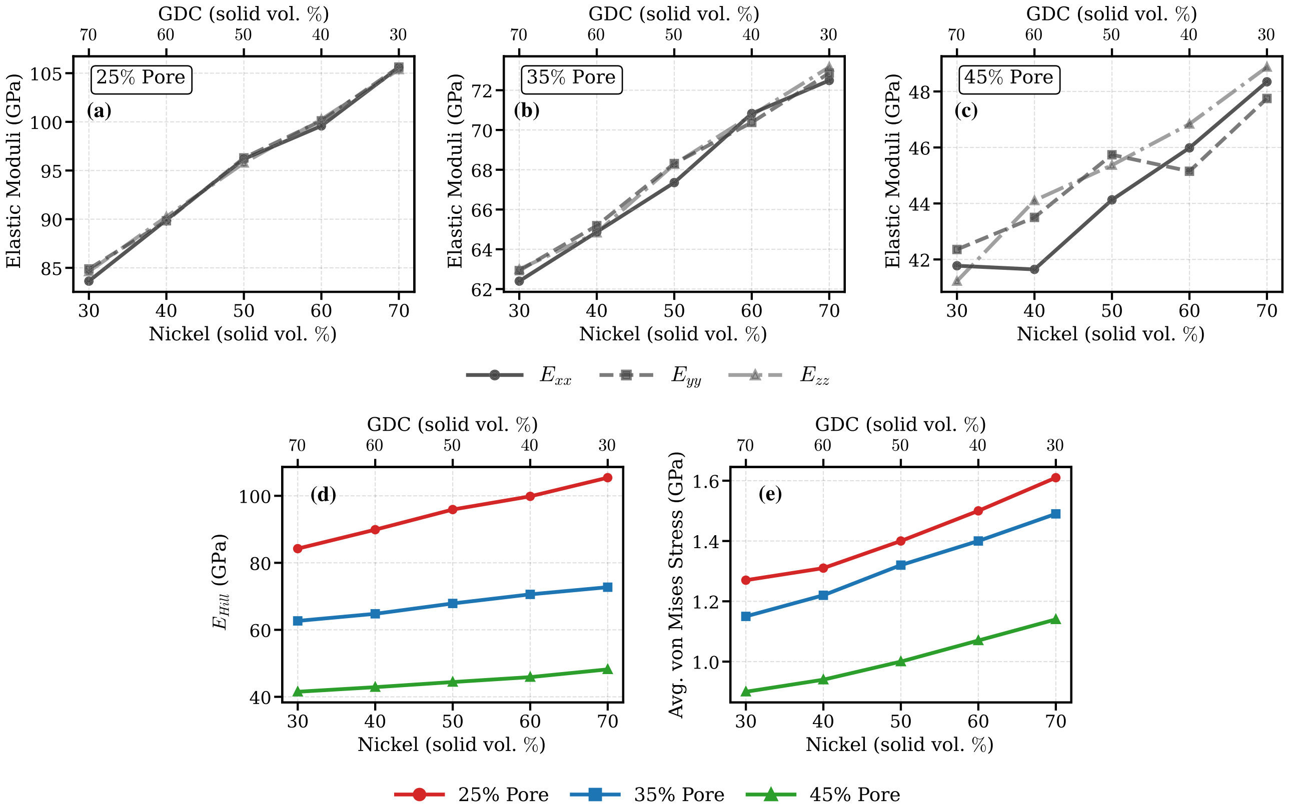

Fig. 2 | Effect of porosity and nickel/gadolinium-doped ceria (Ni/GDC) solid volume fractions (solid vol. %) on effective mechanical properties and stresses. Directional elastic moduli (E_{xx}, E_{yy}, E_{zz}) are shown for pore volume fractions of **a** 25%, **b** 35%, and **c** 45%. **d** Hill average elastic modulus (E_{Hill}), and **e** average von Mises stress are also presented for varying porosity and solid volume fractions.

Table 1 | Properties of the materials used in the mechanical simulations

Phase	Elastic modulus *E* (GPa)	Poisson's ratio *ν*	Thermal expansion coefficient α_θ (K^{-1})
Ni	200[85]	0.31[85]	16.00 × 10^{-6} [86]
GDC	120[87]	0.33[87]	12.96 × 10^{-6} [88]

microstructure is replaced by an equivalent homogeneous continuum, enabling a systematic evaluation of the effective mechanical properties and their evolution during aging as a function of the initial microstructural configuration. Effective mechanical properties of porous Ni-GDC anodes, comprising directional elastic moduli and Hill's average, were extracted from the initial synthetic microstructures of groups A, B, and C to establish structure-property correlations. The directional elastic moduli (E_{xx}, E_{yy}, and E_{zz}) for groups A, B, and C are shown in the Fig. 2a–c. For groups A and B, the directional moduli for a given composition are clustered closely, indicating a nearly isotropic elastic response. In contrast, group C (45% porosity) exhibits pronounced elastic anisotropy (Fig. 2c). As shown in Fig. 2d, the Hill average modulus (E_{Hill}) decreases linearly with increasing porosity, declining from 84.23–105.41 GPa for group A (25% porosity) to 41.51-48.19 GPa for group C (45% porosity). This tendency is consistent with computational studies on reconstructed Ni-YSZ anodes and porous media models, which reported a reduction in the elastic modulus with increasing porosity, in accordance with Gibson-Ashby's scaling laws[53–55]. At fixed porosity, E_{Hill} increases with increasing Ni solid volume fraction in all groups. Specifically, E_{Hill} increases from 84.23 to 105.41 GPa in group A, from 62.66 to 72.72 GPa in group B, and from 41.51 to 48.19 GPa in group C as the Ni/GDC solid volume fraction changes from 30/70 to 70/30. This behavior results from the higher elastic modulus of Ni (200 GPa) in comparison to GDC (120 GPa), as shown in Table 1.

Influence of initial microstructure on mechanical response

In order to approximate the mechanical constraints imposed on the anode in an SOFC stack, a boundary condition setup was employed, similar to the approach used in the work of Elmoghazy et al.[34]. The interface between the anode and electrolyte was fully fixed ($(u_x, u_y, u_z) = (0, 0, 0)$), the interface between the anode and interconnect was constrained only in the normal direction ($u_z = 0$), while the lateral surfaces were constrained in their normal displacement ($u_n = 0$) to account for the confinement by neighboring cells. Contrary to the strain-controlled homogenization framework employed to estimate the effective elastic moduli (Microstructure quantification section), the stack-level boundary condition setup enables the coupled evolution of stress and strain resulting from thermal expansion and mechanical confinement, thereby providing a more physically representative evaluation of the internal mechanical response. The von Mises stress is utilized here as an equivalent scalar measure of the multiaxial thermomechanical stress state, thereby enabling a quantitative comparison of stress levels and their spatial distribution across different microstructures and aging states. It is used solely as an indicator of the overall stress state and is not intended to predict fractures, failure, or damage. Figure 2e shows the average von Mises stress under the applied stack boundary conditions and thermal expansion, for different porosities and Ni/GDC solid volume fractions. The average von Mises stress is defined as $\langle\sigma_{\mathrm{vM}}\rangle = \frac{1}{V}\int_V \sigma_{\mathrm{vM}}(\mathbf{x})\,dV$. Overall, the average von Mises stress decreases with increasing porosity, declining from a maximum of 1.61 GPa for group A (25% porosity) to 0.90 GPa for group C (45% porosity). At fixed porosity, the average von Mises stress increases with Ni content in all groups: from 1.27 to 1.61 GPa in group A, from 1.15 to 1.49 GPa in group B, and from 0.90 to 1.14 GPa in group C, with the Ni/GDC ratio changing from 30/70 to 70/30. As expected, these trends largely correspond to those of the Hill average elastic modulus. The relatively high stress values predicted in this study are attributed to the purely elastic material model assumption. In practice, part of the stress would be relaxed

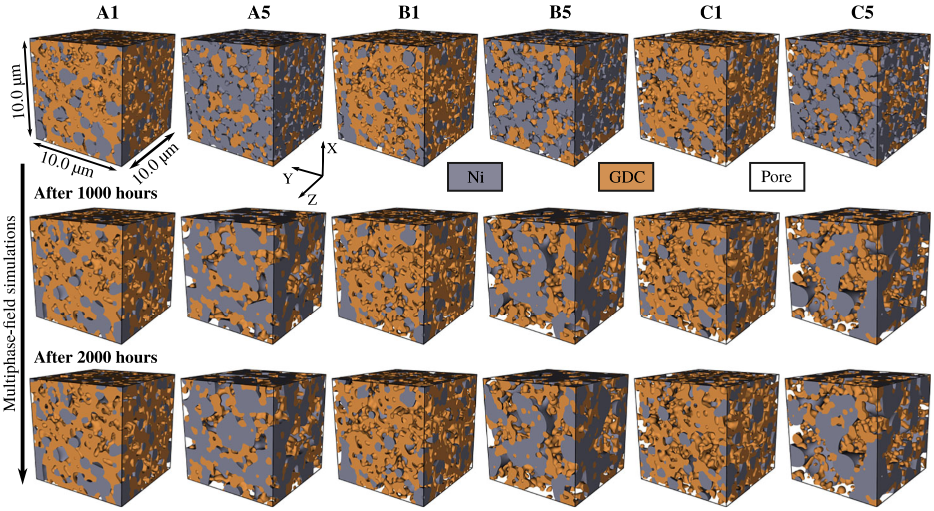

Fig. 3 | Morphological evolution of the pristine synthetic 3D nickel-gadolinium doped ceria (Ni-GDC) anode microstructures after 1000 and 2000 hours of aging for selected initial configurations (A1, A5, B1, B5, C1, C5) predicted from multiphase-field simulations.

by inelastic deformation or damage mechanisms. Therefore, the present stress values should primarily be interpreted comparatively when evaluating differences between microstructures. It is observed that, on account of the similar evolution of E_{Hill} and the average von Mises stress, i.e., increase with Ni content and decrease with porosity, it can be approximated that the thermal eigenstrain remains nearly constant across all configurations. This insensitivity can be largely attributed to the relatively small differences in the thermal expansion coefficients of Ni and GDC (Table 1), thereby reducing the influence of solid volume fraction variations on the overall thermal eigenstrain.

Evolution of microstructure and particle size during aging under varying initial configurations

All pristine synthetic Ni-GDC microstructures were employed as inputs for multiphase-field aging simulations performed for 2000 hours, with properties evaluated at 50-hour intervals. To comprehensively characterize the anode degradation, the analysis focused on the temporal evolution of the mean particle diameters of Ni, GDC, and pores; electrochemically-relevant metrics such as TPB and DPB densities as well as phase tortuosities; and effective mechanical properties like directional elastic moduli, Hill average elastic modulus, and critical volume fraction. The objective here is to quantify the influence of different initial configurations on the degradation of these key properties. A detailed analysis of the correlations between the initial configurations of the microstructure and the degradation of its properties enables the targeted optimization of the initial microstructures, ultimately leading to improved durability and efficiency of SOFCs. Figure 3 shows the 3D microstructure evolution of selected configurations (A1, A5, B1, B5, C1, C5) after aging times of 1000 h and 2000 h. Microstructural evolution directly affects the electrochemical reaction sites, the transport of ions, electrons, and gases, and thus the long-term stability of the anode. Experimentally, aging-induced coarsening of Ni and GDC has been widely reported and is reflected by an increase in the mean particle size[5,8,9].

Figure 4a–c depicts the evolution of the mean Ni particle diameter for porosity groups A, B, and C. In all microstructural configurations, Ni coarsening is most pronounced during the early stages of aging and slows considerably at later stages, in agreement with experimental observations[8] and simulations[19,24]. For all porosity groups, the relative increase in the mean Ni particle diameter, as expected, increases with increasing Ni solid volume fraction. The largest particle growth after 2000 aging hours is observed in A5 at 46.6% (0.762 to 1.117 μm), B5 at 54.8% (0.768 to 1.189 μm), and C5 at 56.7% (0.748 to 1.172 μm) with Ni volume fractions of 52.71%, 45.26%, and 38.60%, respectively. It is noteworthy that the highest relative growth occurs in configuration C5, despite its lower Ni volume fraction. This behavior can largely be attributed to the combined effect of higher pore content (44.9% vol.) and lower inhibition by the GDC network (vol. 16.50%) in conjunction with the significantly faster surface diffusivity of Ni in comparison to interfacial diffusivity (five orders of magnitude[25]), promoting rapid particle coalescence among the nickel particles and thus a higher increase in the mean particle diameter. Figure 4d–f shows the evolution of the mean GDC particle diameter for porosity groups A, B, and C. In contrast to Ni, GDC exhibits a much slower and more gradual coarsening behavior over time, reflecting its significantly lower diffusivity, about five orders of magnitude lower than that of Ni[25]. Across all porosity groups, the relative increase in the mean GDC particle diameter increases with increasing GDC solid volume fraction, similar to the trend observed for Ni. Minor differences among the curves at different solid volume fractions within a given group arise from slightly different initial GDC particle sizes of those respective configurations. After 2000 aging hours, the largest particle growth is observed for A1 at 17.3% (0.514 to 0.603 μm), B1 at 8.9% (0.505 to 0.550 μm), and C1 at 5.6% (0.503 to 0.531 μm), with GDC volume fractions of 52.57%, 45.28%, and 38.34%, respectively. The largest relative growth in GDC is observed in configuration A1, which has the highest GDC volume fraction. Given the smaller particle size, strong percolation, and relatively low diffusivity of GDC, particle coarsening is primarily dependent on the volume fraction in the investigated 2000-hour aging time, rather than the porosity and inhibition by the nickel network. Figure 4g–i displays the evolution of the mean pore diameter across A, B, and C porosity groups. Porosity evolves in accordance with the rearrangement and coalescence of solid particles in the structure. As particle coalescence progresses, the pore network becomes increasingly connected - also reflected in the decreasing pore tortuosity as shown in Fig. 7g–i - resulting in an increasing mean pore size over time. During early aging, pore evolution follows Ni coarsening closely, due to the rapid growth of Ni. In later stages, the continuing, but slower, coarsening of GDC determines the further pore evolution. The largest growth in pore size after 2000 aging hours is observed in A5 at 128.8% (0.320–0.732 μm), B5 at 119% (0.397–0.870 μm), and C5 at 102.7% (0.475–0.963 μm), with pore volume fractions of approximately 25%, 35%, and 45%, respectively. As the porosity varies between groups A, B, and C, their initial pore size distributions also differ correspondingly. As a result, group C with higher porosity displays the largest absolute pore diameters, while group A of lower porosity exhibits the largest relative pore growth, reflecting substantial enlargement of initially smaller and more restricted pores despite smaller final absolute sizes.

Electrochemical performance-related microstructural properties degradation

The evolution of the total TPB density for porosity groups A, B, and C is shown in Fig. 5a–c. In accordance with the rapid coarsening of Ni during early aging, the TPB density decreases sharply at the initial stage and slows down considerably over longer durations. Overall, it can be seen that the

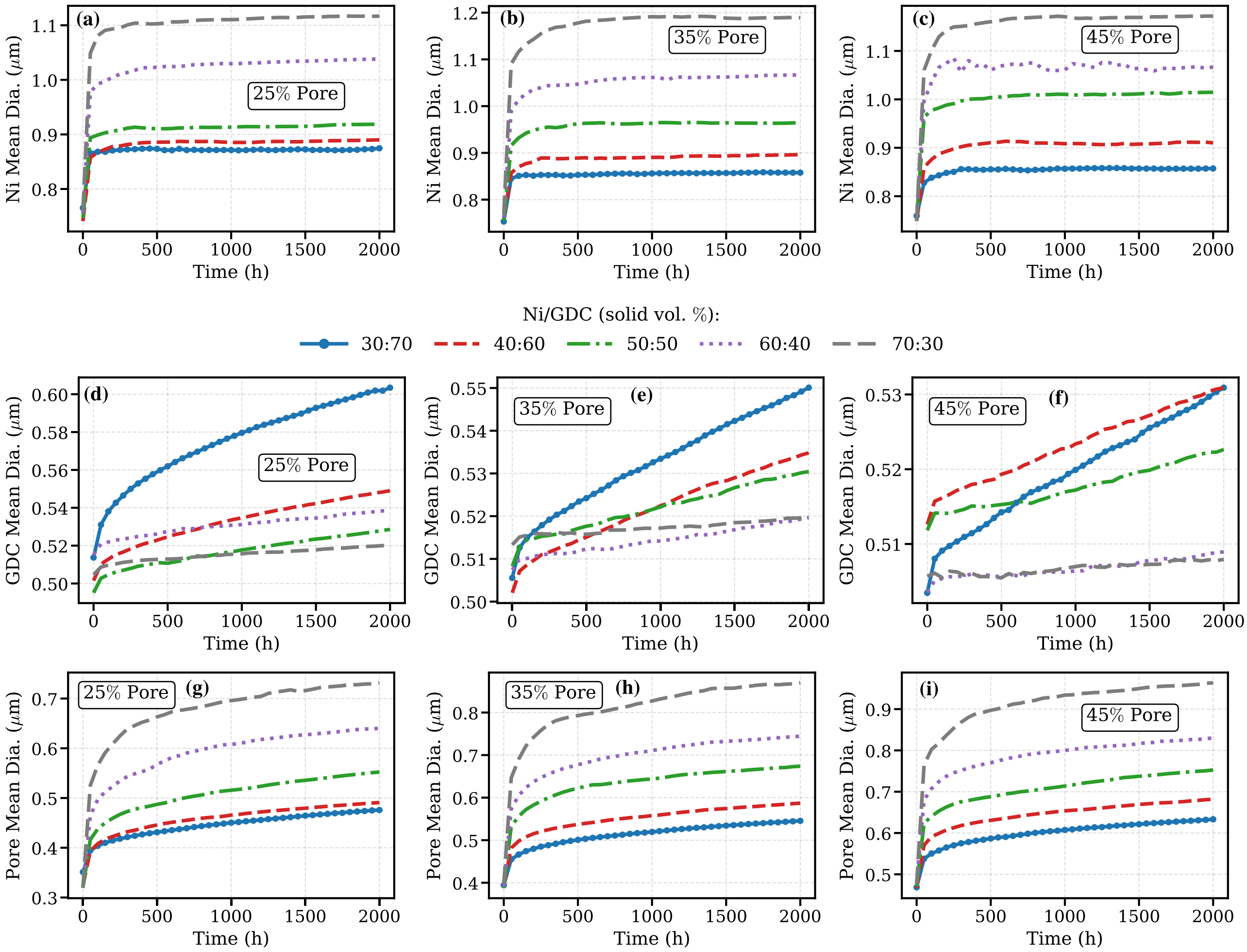

Fig. 4 | Evolution of the mean diameter over 2000 hours of aging from multiphase-field simulations. a–c nickel, **d–f** gadolinium-doped ceria (GDC), and **g–i** pore phases at porosity groups of 25%, 35%, and 45%, respectively, across solid volume fractions (solid vol. %) of nickel/gadolinium-doped ceria (Ni/GDC).

TPB evolution shows a qualitatively inverse correlation to the mean Ni and GDC particle diameter evolution. After 2000 hours of aging, the TPB density decreases by 43.8% to 69.4% relative to the respective initial values, indicating a significant loss of electrochemical reaction sites and a corresponding degradation in cell performance. At a fixed porosity, a higher Ni solid volume fraction leads to relatively greater TPB degradation and lower absolute TPB densities after aging. Across all porosity groups, the structures with high porosity (group C) exhibit the lowest TPB densities after 2000 hours of aging, while the structures with low porosity (group A) display comparatively higher values. Considering both the initial TPB density and long-term stability, configurations A2 (Ni vol. 29.77%, GDC vol. 45.33%) and A3 (Ni vol. 37.60%, GDC vol. 37.99%) show the best properties, with TPB densities decreasing from initial values of 4.5, 4.98 μm^{-2} to values of 1.87 and 1.85 μm^{-2}, respectively, after 2000 aging hours. Competing mechanisms of Ni and GDC coarsening in conjunction with wettability or dewetting behavior at Ni/GDC interfaces enhance the complexity of morphological evolution. As demonstrated in our previous work, interfacial energy configurations in the Ni-GDC-Pore system with wetting behavior can mitigate TPBs loss and enhance microstructural stability during long-term operation[24]. Figure 6 shows the evolution of the total triple-phase boundary from the initial state to 2000 hours of aging for selected configurations (A3, B3, C3). Figure 5d–f illustrates the DPB density evolution for porosity groups A, B, and C. Across all configurations, DPB density decreases monotonically with aging, resulting in an overall reduction of 14.6% to 18.9% from the initial values after 2000 h of aging. Porosity groups B (35%) and C (45%) maintain higher and nearly identical DPB densities over the entire aging period, in line with the higher initial values. Within each porosity group, a higher GDC solid fraction is also associated with higher DPB densities after long-term aging. Kishimoto et al.[56] have demonstrated through sensitivity analyses at 700 °C that the electrochemical reaction at the DPB is the rate-limiting step in ceria-based electrodes, indicating that increasing the DPB density is more effective for improving performance than increasing species transport. In accordance with these results, configurations B1 and C1 exhibit the highest DPBs both in their pristine state (2.02 and 2.02 μm^{-1}) and after 2000 hours of aging (1.70 and 1.72 μm^{-1}), implying their preference in terms of both initial performance and long-term stability.

To quantify effective electronic, ionic, and gas transport pathways, the time evolution of the mean tortuosity of the Ni, GDC, and pore phases is presented in Fig. 7. The evolution of nickel mean tortuosity for porosity groups A, B, and C is shown in Fig. 7a–c. Multiple configurations (A1, B1, C1, C2) were not included, as nickel is non-percolating in the initial structures. Configuration C3 (Ni vol. 27.58%, GDC vol. 27.34%) was initially percolated, with a mean nickel tortuosity of 27.94; however, it becomes non-percolating over aging due to a very high initial directional tortuosity value of 54 in the x-direction. Although percolation persists in the y- and z-directions, the loss of connectivity in the x-direction results in a non-percolated mean value. These results indicate that microstructures with high initial tortuosity values are prone to forming nickel islands, particularly at low nickel volume fractions. Configuration A2 (Ni vol. 29.77%, GDC vol. 45.33%) exhibits a significant increase in nickel tortuosity from 21.12 to 29.93 after 2000 h. In configurations with low Ni and high GDC volume

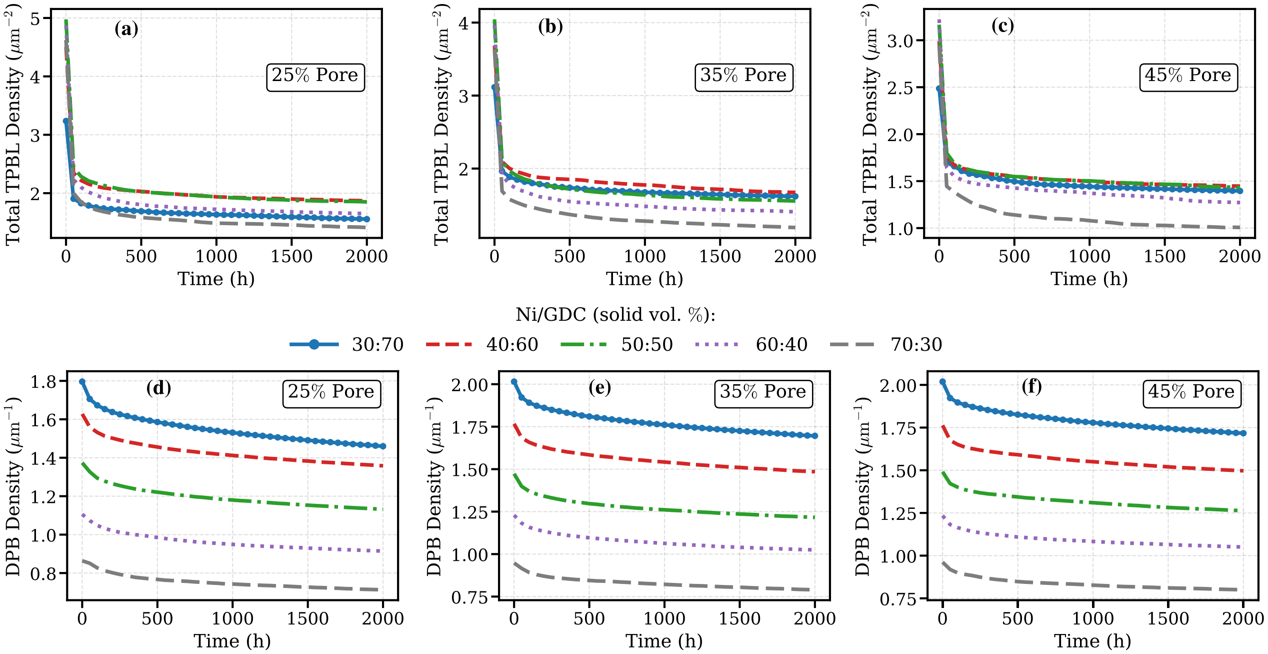

Fig. 5 | Evolution of electrochemical reaction sites over 2000 hours of aging from multiphase-field simulations. a–c total triple-phase boundary lines (TPBL) density, **d–f** double-phase boundary (DPB) density at porosity groups of 25%, 35%, and 45%, respectively, across solid volume fractions (solid vol. %) of nickel/gadolinium-doped ceria (Ni/GDC).

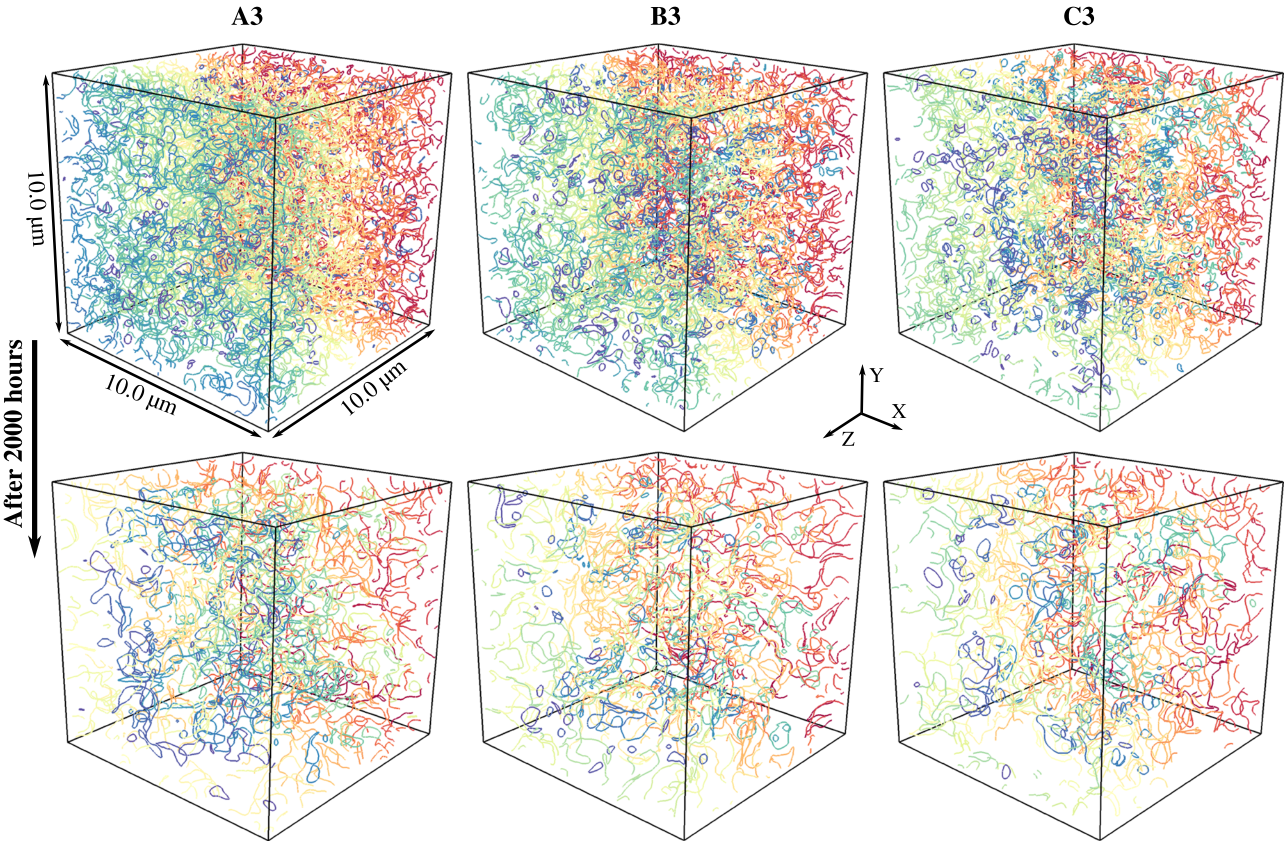

Fig. 6 | Total triple-phase boundary at initial and after 2000 hours aging for porosity groups of 25% (A3), 35% (B3), and 45% (C3), respectively, from multiphase-field simulations, with color-coded triple-phase boundary (TPB) segments.

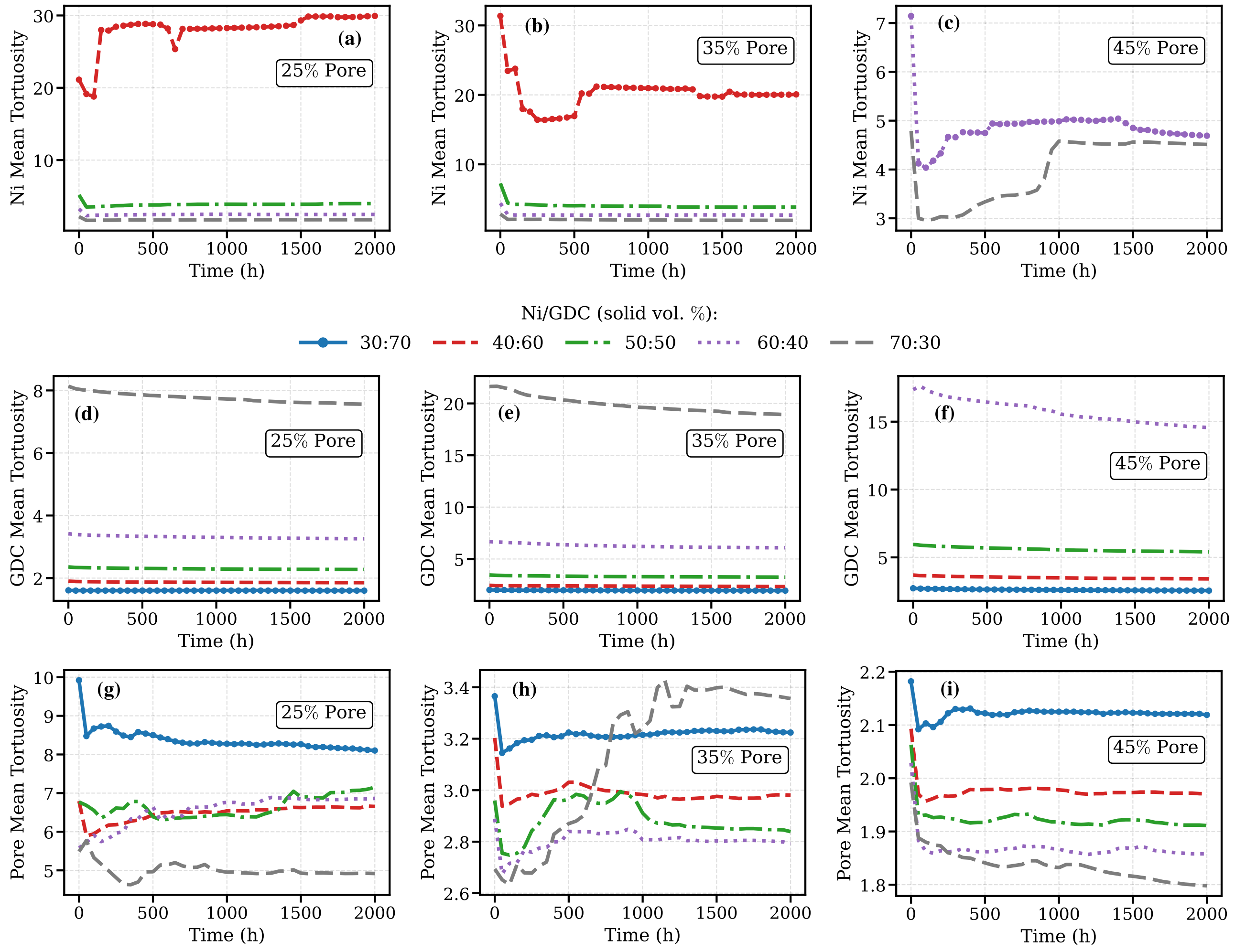

Fig. 7 | Evolution of mean tortuosity over 2000 hours of aging from multiphase-field simulations. a–c nickel (Ni), **d–f** gadolinium-doped ceria (GDC), and **g–i** pore phases at porosity groups of 25%, 35%, and 45%, respectively, across solid volume fractions (solid vol.%) of nickel/gadolinium-doped ceria (Ni/GDC).

fractions, nickel coarsening can lead to encapsulation of Ni particles by the GDC network in some areas, restricting further coalescence, but forming the isolated Ni regions. This significantly increases tortuosity, as electron transport paths must circumnavigate the high density of GDC networks. Such microstructural configurations are highly sensitive to local morphological changes, where minor connectivity losses can cause large tortuosity variations. Increased tortuosity, resulting in an increased isolated Ni volume fraction, is reported in the literature[57]. The increase in tortuosity is most pronounced during early aging, consistent with rapid nickel coarsening, but shows various discontinuities (absent in particle size evolution). It could be due to tortuosity being highly sensitive to local variations in particle connectivity or isolation, unlike volume properties (which are less affected by such local events), where local particle isolation or percolation changes can significantly alter the values.

Configurations B2 (Ni vol. 25.71%, GDC vol. 39.13%) and C4 (Ni vol. 32.85%, GDC vol. 21.96%) show an initial decrease followed by a gradual increase and eventual stabilization of tortuosity. Despite lower nickel content in the B2 structure than in A2, reduced GDC network and higher porosity promote better connectivity initially as particle coalescence starts, but over time, the reduction in particle number and formation of nickel islands could result in increasing tortuosity values. Despite containing a similar nickel content to A2, the C4 structure, with its higher porosity of 45%, exhibits better initial properties and a similar evolution to the B2 structure. These results demonstrate that nickel tortuosity depends not only on Ni content, but also on GDC fraction and porosity, consistent with prior studies stating that both solid fraction and porosity control percolation thresholds[58]. At higher nickel contents, the correlation is noticeably weaker, and an increasing particle size of Ni does not necessarily result in increased tortuosity of nickel over time. Consistent with previous studies that investigated structures with nickel contents of 20%, 25%, and 33% for the Ni-YSZ system, the high nickel content of 33% resulted in a tortuosity value that remained nearly invariant over time[59].

Electron transport is often not the rate-limiting process in SOFC anodes and may therefore make Ni tortuosity values seem less critical. In Ni-GDC anodes, the GDC phase also exhibits electronic conductivity, which is one to two orders of magnitude higher than its ionic conductivity, further reducing the likelihood of electron transport limiting electrochemical reactions. Consequently, the distribution of electrochemical activity is primarily determined by ionic conduction rather than electronic transport[60]. From this standpoint, nickel tortuosity may not be a primary design focus in Ni-GDC anodes. In cases where the nickel network becomes non-percolating, the effective electronic conductivity is predominantly controlled by the GDC phase. Nevertheless, the assumption that the entire DPB is electrochemically active remains subject to debate; instead, reactions may be localized around TPB regions. This effect can become more pronounced at lower operating temperatures due to the lower electronic conductivity in the GDC phase. Consequently, higher TPB and DPB densities, together with lower tortuosity of the Ni and GDC phases, may remain desirable in certain cell designs and operating conditions. Therefore, the sensitivity of electrode performance to all microstructural properties in terms of initial configurations and degradation remains important, as it determines the parameters that need to be prioritized for microstructural optimization. Findings and insights gained from this study are likely to be useful in future efforts to enhance the microstructure of electrodes, as well as in cell-level modeling and TLM for electrochemical performance.

The evolution of GDC tortuosity for porosity groups A, B, and C is depicted in Fig. 7d–f. Configuration C5 was excluded due to the initial non-percolating GDC phase. For all other configurations, GDC tortuosity displays only a slight decrease over the aging period, indicating that the ionic and electronic transport pathways remain largely stable with respect to their initial states. Such behavior correlates with the slow coarsening kinetics of GDC, as reflected in only minor increases in the mean particle diameter. While local coalescence of GDC particles occurs, the degree of coalescence remains insufficient to result in particle isolation or loss of percolation. Instead, the low diffusivity and surface energy of GDC promote the formation of smoother, more continuous networks, thereby preserving long-range connectivity over time. Kishimoto et al.[56] investigated the sensitivity of electrode area-specific resistance (ASR) to key microstructural parameters, including DPB density, GDC tortuosity, and mean pore size. Their analysis concluded that ASR is most sensitive to DPB density, with variations spanning nearly two orders of magnitude, while changes in GDC tortuosity and pore size resulted in comparatively small ASR variations within the same order of magnitude. Furthermore, increased DPB density remains the most effective strategy for improving performance, with a 10% increase in DPB density resulting in a 10% reduction in ASR. Finally, the increase in GDC tortuosity needs to be limited to prevent an increase in ohmic losses associated with ion conduction.

Based on the aforementioned results, several conclusions could be drawn. In the initial microstructures, GDC volume fractions between 30.52% and 52.37% resulted in well-percolated transport networks, with GDC tortuosity dropping from 3.69 to 1.61. Given the role of GDC in electrochemical reactions, as well as ionic and electronic transport pathways, configurations with non-percolating or low Ni content might still be viable depending on the cell design. In this regard, configurations B1 (Ni vol. 19.67%, GDC vol. 45.25%), B2 (Ni vol. 25.71%, GDC vol. 39.13%), and C1 (Ni vol. 16.78%, GDC vol. 38.34%) prove to be favorable, as they exhibit high initial DPB densities and modest aging degradation (B1: 2.02 to 1.70, B2: 1.77 to 1.49, C1: 2.02 to 1.72 μm^{-1}) along with low and stable GDC tortuosity (B1: 2.02 to 1.95, B2: 2.46 to 2.36, C1: 2.72 to 2.55). Previous studies have shown that ceria-based electrodes hold the potential to operate as SOFC anodes without a secondary electronic phase. Chueh et al.[61] demonstrated this for single-phase ceria, and Nakamura et al.[62,63] showed the same for micrometer-sized pure GDC. In addition to DPB density and GDC tortuosity, if Ni-related metrics are prioritized, such as TPB density and Ni tortuosity, configuration B2 may be preferable. Compared to B1 (3.12 to 1.62 μm^{-2}) and C1 (2.49 to 1.40 μm^{-2}), configuration B2 exhibits higher TPB density and lower degradation (3.68 to 1.67 μm^{-2}) in addition to being the only configuration among the three with a percolated Ni network. Nevertheless, simultaneous maximization of both the electrochemical reaction sites (TPBs and DPBs) and minimization of the tortuosity of the Ni and GDC transport networks is difficult, as these microstructural properties are inherently coupled and often compete with each other. Increasing and balancing solid volume fractions of Ni and GDC tends to increase TPB density but is likely to decrease DPB density. Conversely, high GDC volume fractions do not necessarily lead to the highest DPB densities, as limited pore volume could constrain DPB formation. Furthermore, efficient transport generally favors higher volume fractions of each phase, which further competes with the need for substantial interfacial reaction sites. Figure 7g–i shows the evolution of pore tortuosity for porosity groups A, B, and C. Group C (45% porosity), with an already low initial pore tortuosity, shows a moderate but overall decreasing pore tortuosity across all Ni/GDC solid volume fractions with aging. Pore tortuosity correlates well with initial pore size and its evolution, with larger pores promoting improved connectivity and lower tortuosity. These findings are consistent with the phase-field studies by Chen et al.[14], reporting that prolonged coarsening in Ni-YSZ systems can enhance gas transport through the pore phase. In contrast, groups A and B across different Ni/GDC compositions show rather discontinuous and non-monotonic trends in pore tortuosity. In these systems with lower porosity, the correlation between pore size and tortuosity is noticeably weaker, and an increase in pore size does not necessarily correspond to a reduction in tortuosity over time. This behavior reflects the complex microstructural evolutions of Ni and GDC coarsening and interfacial dynamics, thus making direct correlations between morphological evolution and pore tortuosity less straightforward. Furthermore, microstructures with lower porosity are more sensitive to local particle redistributions occurring during aging than highly porous systems. Overall, pore tortuosity, similar to GDC tortuosity, shows no significant changes during aging across all configurations (except for configuration A1), indicating that gas diffusion pathways remain largely stable compared to their initial state.

Mechanical performance-related effective properties degradation

Evolution of elastic properties for porosity groups A, B, and C is shown in Fig. 8a–l. All configurations show an overall reduction in elastic properties over aging. An increase in pore size and shape change generally results in a degradation of mechanical strength and a reduction in stiffness. For example, in configuration A1, the effective directional moduli E_{xx}, E_{yy}, and E_{zz} decrease from 83.63, 84.89, and 84.62 GPa to 78.77, 80.27, and 80.39 GPa, respectively, while Hill average elastic modulus E_{Hill} decreases from 84.23 to 79.77 GPa as the mean pore diameter increased from 0.351 to 0.476 μm over 2000 hours of aging. Figure 8a–c depicts the evolution of the Hill average elastic modulus E_{Hill} for porosity groups A, B, and C. For all configurations, E_{Hill} shows a pronounced initial decline, corresponding to rapid Ni coarsening in the early stages, followed by a gradual decline or a nearly constant value at longer aging times. The overall reduction in E_{Hill} ranges from 5.30% to 14.48%, with the highest deterioration observed in the high porosity group C and the lowest in group A. Figure 8d–l shows the evolution of the effective directional elastic moduli (E_{xx}, E_{yy}, E_{zz}) for porosity groups A, B, and C. The moduli show a sharp initial decline, followed by a slower decline or near stabilization at later stages, except for configurations B5 and C5, consistent with the trends in the Hill average elastic modulus. The correlation between the increase in mean pore diameter and the reduction in effective directional elastic moduli is weaker for configurations B5 and C5. Although the pore size increases monotonically in these structures, the discontinuous evolution of pore tortuosity in B5 and Ni tortuosity in C5, arising from local particle rearrangements, might strongly influence the evolution of the directional moduli. Overall, the effective directional elastic moduli decrease between 5.7% and 18.9% for all configurations. Group C, with high porosity, shows the largest relative decrease, while group A shows the lowest. Configurations with higher Ni content, higher porosity, and less inhibition by the GDC network (e.g., B5 and C5) also display increased anisotropy during aging. In configuration C5, for example, the effective directional elastic moduli decrease by 0.9%, 1.9%, and 17% along the x, y, and z directions, respectively, after 2000 hours of aging. In the work of Brus et al.[64], it was shown that long-term SOFC operation of a Ni-YSZ anode resulted in strong anisotropy in the anode microstructure. An initially isotropic anode, after prolonged operation of 3800 hours, exhibited strong anisotropy, particularly in the nickel and pore phases of the investigated Ni-YSZ anode. As possible causes for the anisotropies, nickel migration, growth, and coarsening were mentioned. Also, they highlighted the importance of credible numerical simulations of SOFCs accounting for these anisotropies. Liu et al.[33] reported an increase in elastic properties during the sintering stage of Ni-YSZ anode fabrication, as progressive densification resulting in reduced porosity enhances elastic properties with sintering time. The current study demonstrates that during long-term aging of Ni-GDC anodes, microstructural coarsening and pore evolution result in a decrease in elastic properties. Overall, the elastic properties and the evolution of these properties over time are determined by the combined effects of porosity, Ni/GDC volume fractions, pore size and shape, as well as the connectivity of the phases.

A common degradation mechanism in SOFCs is delamination at the electrode-electrolyte interface, which compromises cell integrity and leads

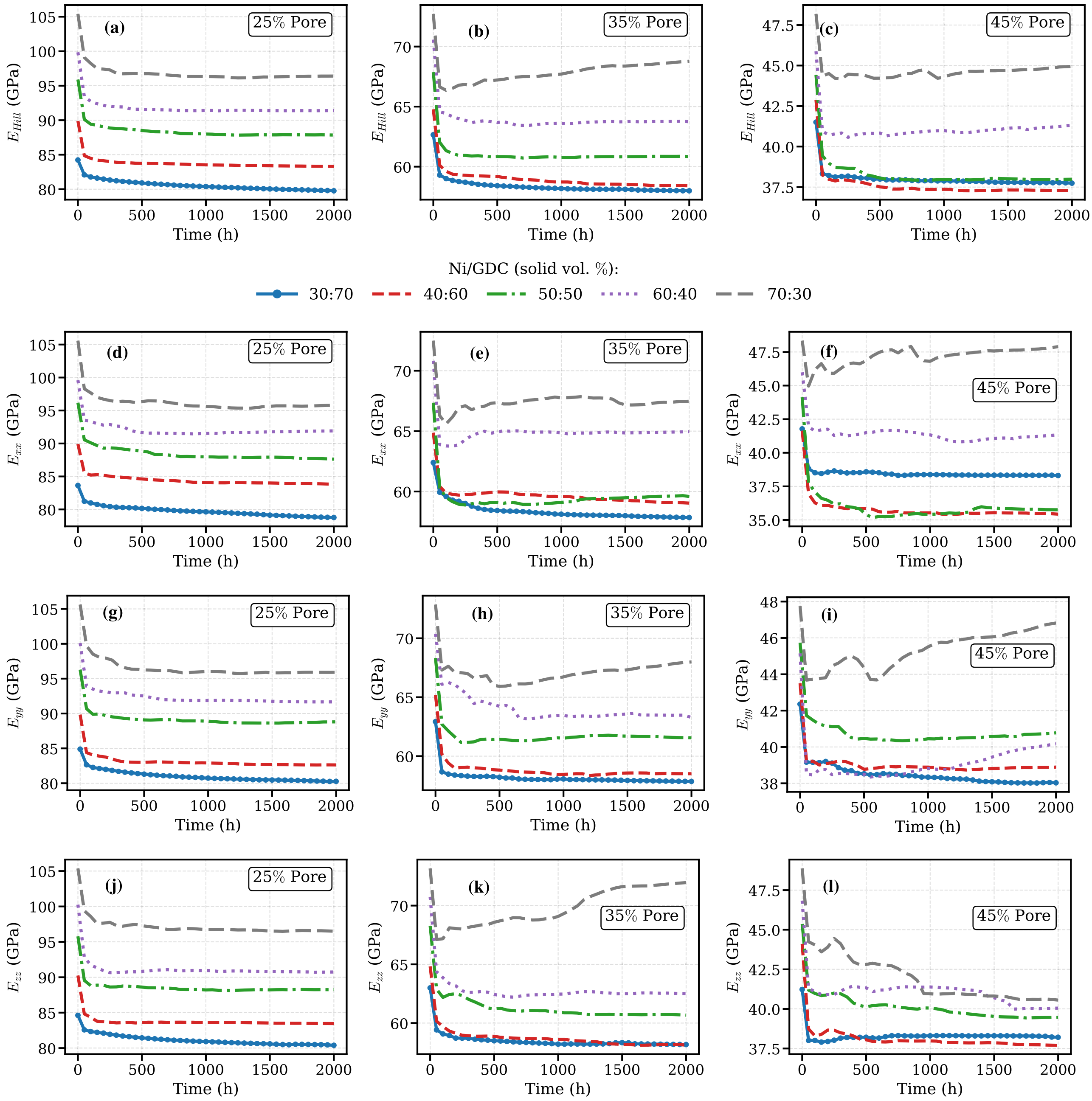

Fig. 8 | Evolution of elastic properties over 2000 hours of aging from multiphase-field simulations. a–c Hill average elastic modulus (E_{Hill}), and effective directional elastic moduli (**d–f**) E_{xx}, **g–i** E_{yy}, j–l E_{zz} for porosity groups of 25%, 35%, and 45%, respectively across solid volume fractions (solid vol. %) of nickel/gadolinium-doped ceria (Ni/GDC).

to performance degradation. This damage is primarily caused by thermo-mechanical stresses arising from different thermal expansion coefficients of the electrode components and the electrolyte; Consequently, the composition of the anode has a strong influence on the resulting stress distribution. In addition, partial performance degradation during operation is often associated with some partial breakup of Ni/YSZ or Ni/GDC interphases, which disrupts ionic and electronic transport pathways and reduces the density of three-phase boundaries. Figure 9a–f shows the evolution of the average von Mises stress and the CVF under the applied stack boundary conditions. From a mechanical standpoint, the CVF quantifies the fraction of the microstructure exposed to stresses exceeding a threshold level. The CVF is defined as $\mathrm{CVF} = \frac{1}{V_{\mathrm{tot}}} \int_{V(\sigma_{\mathrm{vM}} > \sigma_{\mathrm{threshold}})} \mathrm{d}V$, where the threshold value $\sigma_{\mathrm{threshold}}$ is taken as the average von Mises stress of the pristine state of the corresponding configuration. This microstructure-specific normalization accounts for intrinsic differences in stiffness, phase connectivity, and constraint among microstructures, enabling the CVF to reflect aging-induced stress localization with respect to the threshold of each configuration, rather than an absolute stress threshold applied uniformly to all structures. As microstructure coarsening progresses, the internal load distribution also changes: Stress concentrations are reduced in areas where sharp curvatures and small features vanish, while other regions carry a larger proportion of the load. These redistributions are also influenced by initial Ni/GDC solid volume fractions, porosity, and the evolution of particle sizes and shapes, and directly affect both overall stress and localized stress concentrations. As shown in Fig. 9a–f, the coarsening of the microstructure over aging results in a significant redistribution of local stress fields and large changes in global loading conditions. Consequently, both the average von Mises stress and CVF exhibit similar qualitative trends across configurations.

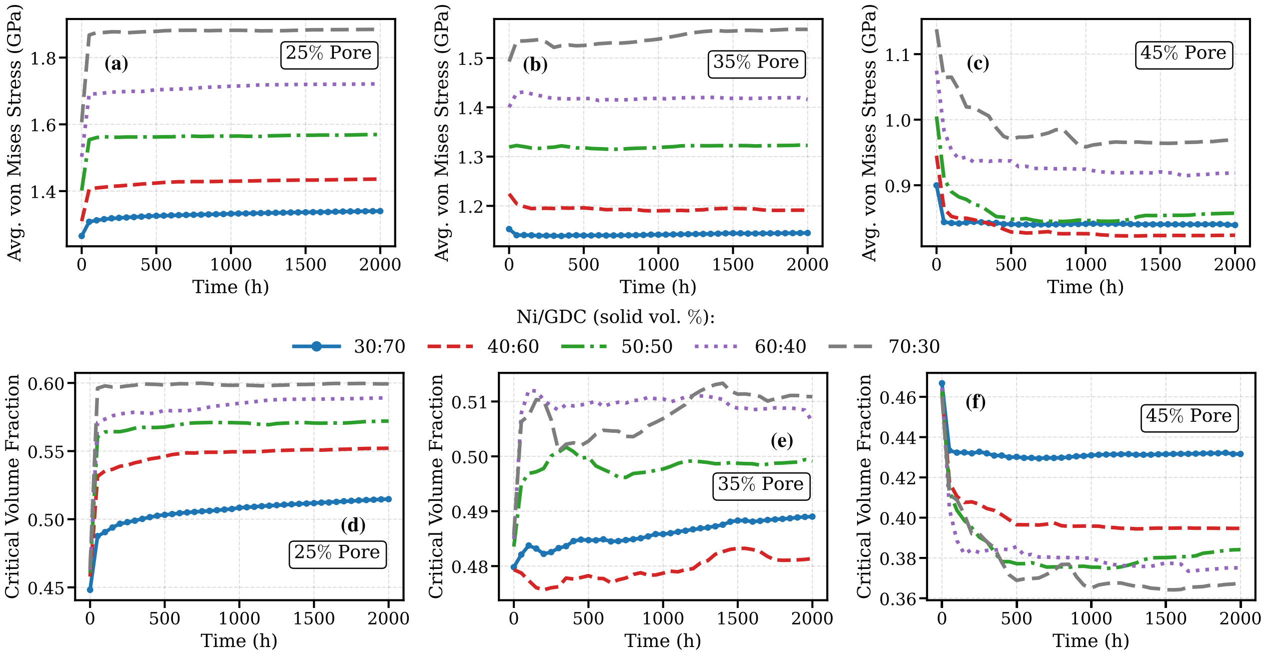

Fig. 9 | Evolution of mechanical response over 2000 hours of aging from multiphase-field simulations. a–**c** Average von Mises stress, and **d**–**f** critical volume fraction for porosity groups of 25%, 35%, and 45%, respectively, across solid volume fractions (solid vol. %) of nickel/gadolinium-doped ceria (Ni/GDC).

In group A (low porosity), both the average von Mises stress and the CVF increase with aging across all Ni/GDC solid volume fractions, indicating an enhancement of thermally induced stresses resulting from the coefficient of thermal expansion (CTE) mismatch between Ni and GDC. These results suggest that high-density Ni-GDC anodes experience elevated stress levels during long-term operation. From a mechanical integrity standpoint, an increase in average von Mises stress, particularly when coupled with an increase in CVF, indicates an overall elevation of the internal stress state and stress concentration within the microstructure. This behavior might be attributed to the high effective stiffness (E_{Hill}) and low porosity of the structures, which strongly constrain the thermal-expansion mismatch and limit stress reduction through pores. In the absence of external mechanical loading, stresses resulting solely from thermal expansion might be determined by competing effects of porosity, stiffness, phase connectivity, and local heterogeneity at the interfaces between Ni/GDC and solid/pores, in addition to the primary CTE mismatch. An increase in the Ni volume fraction further increases the stress levels, as the more rigid Ni phase increasingly restricts GDC deformation. For example, in configuration A5, the average von Mises stress increases from 1.61 to 1.88 GPa over aging. The CVF increases from 46.4% to 60.0%, indicating that substantially larger volumes of the microstructure exceed their initial stress threshold. This stress amplification and redistribution caused by coarsening suggest an increased mechanical loading state within the microstructure. Similarly, Xiang et al.[65] simulated thermomechanical stresses arising from the CTE mismatch between Ni and YSZ under operating conditions and external loading. Their results demonstrated that the YSZ volume fraction plays a dominant role in controlling the mechanical strength of the anode, and optimizing the YSZ skeleton during fabrication could significantly improve the resistance to mechanical failure in Ni-YSZ composite anodes.

In the highly porous Ni-GDC anodes of group C, aging enhances stress reduction, as reflected in a systematic reduction in both the average von Mises stress and the CVF across all Ni/GDC compositions. High porosity may promote stress reduction through the pores, allowing the Ni or GDC phase to expand without restriction, and coarsening of the particles under reduced phase constraint might smooth local stress gradients. As a result, a smaller portion of the microstructure is exposed to stresses above the pristine average. For example, in configuration C5, aging resulted in a decrease in the average von Mises stress from 1.14 to 0.97 GPa, and the corresponding critical volume fraction decreases from 46.0% to 36.8%. The decrease in average von Mises stress and CVF over the aging indicates improved tolerance to thermal mismatch strains. However, this improved mechanical stability is achieved at the expense of reduced stiffness (see Fig. 8) and possibly lower electrochemical performance (see Fig. 5). Previous studies have highlighted the strong influence of anode composition and porosity on the thermomechanical behavior in SOFC anodes. Celik et al.[66] numerically investigated the stress distributions in porous Ni-YSZ anodes at the microstructural level and demonstrated that increasing the volume fraction of a particular solid phase (Ni or YSZ) stabilizes thermal expansion and reduces thermo-mechanical stress. They further reported that the lowest stress levels occur at high porosity due to stress reduction through the pores. To further illustrate the local stress redistribution during aging, Fig. 10 shows representative 3D contour maps of the von Mises stress together with the histograms for configurations A5 and C5 in the initial and 2000h aged states. In all cases, the stress field is strongly heterogeneous, with elevated stresses confined to small localized regions, whereas the majority of the microstructural volume remains at comparatively low stress levels. The histograms are strongly right-skewed, showing that very high stress values occur only with very low probability and therefore contribute only weakly to the volume-averaged stress. Aging shifts the stress distribution differently depending on the volume composition. In the A5 configuration, the distribution shifts toward higher stresses and the maximum local stress increases (from 7.76 GPa to 10.30 GPa), while in C5, the distribution shifts toward lower stresses and the maximum stress increases slightly (from 11.55 GPa to 12.57 GPa). The color scale of the stress contour plots is limited to the range of 0 to 4 GPa to enhance the representation of the dominant stress regime, at which the majority of the distribution density is concentrated. These local stress maps and the histograms show that aging is accompanied by a redistribution of stress within the microstructure, as reflected by the change in the probability distribution from the initial to the aged state. A few isolated extreme stress values are also observed, likely associated with very thin neck regions, but these occur with very low probability.

Each microstructure exhibits distinct stiffness, phase connectivity, constraint, and thermal load sharing, resulting in different distributions of thermal stresses depending on the Ni/GDC/porosity balance. In group B (intermediate porosity with 35%), both the average von Mises stress and the CVF remain relatively stable during aging, with only a slight increase

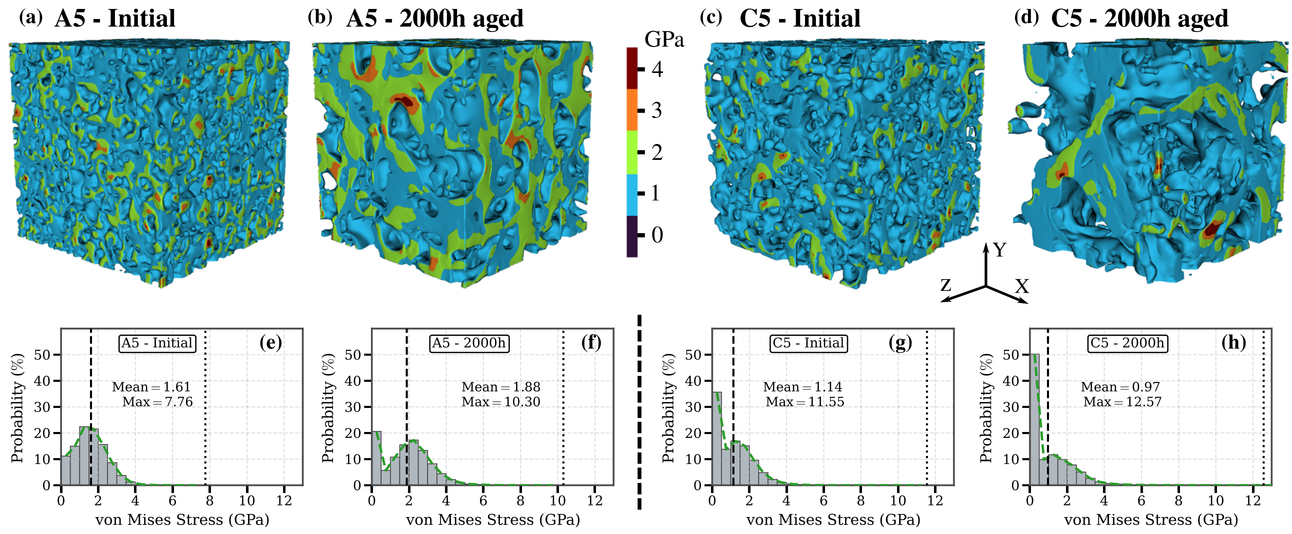

Fig. 10 | Local stress distributions in the initial and 2000h aged microstructures for configurations A5 and C5. a–d contour maps of von Mises stress, and **e–h** stress distributions.

observed in the Ni-rich configuration B5 (CVF: 48.6% to 51.1%; average von Mises stress: 1.49 to 1.56 GPa). These results suggest that a Ni-GDC anode with intermediate porosity offers a mechanically favorable balance: relatively better stiffness values compared to the high porous group (Fig. 8) to sustain load-bearing requirements while limiting stress localization and CVF growth. These results provide an understanding of the possible mechanical degradation in the initial configurations of porous Ni-GDC electrode structures over the aging process as a result of thermal expansion-related stresses and the resulting performance losses, degradation of the SOFC. The current work investigates the overall behavior of the mechanical properties and their deterioration resulting from aging-induced complex morphological evolutions of the 3D Ni-GDC SOFC anode. A detailed analysis of the relevant mechanisms and trends with regard to porosity and evolution within specific groups is beyond the scope of the current research. Nevertheless, these findings provide a basis for future research focusing on more comprehensive investigations.

The rigorously validated digital twin microstructure of the Ni-GDC SOFC anode enabled optimization investigations of anode microstructures using combined electrochemical performance and mechanical integrity metrics in both pristine and aged states. The extended structure generator workflow incorporating sintering-like morphological coalescence produced greatly closer, realistic synthetic microstructures, yielding a global mean absolute percentage error of below 5% over 16 quantitative descriptors. Systematic investigations of fifteen synthetic anode microstructures in the pristine and aged states revealed strong, correlated dependencies of TPB and DPB densities, phase tortuosities, elastic moduli, and stress distributions on Ni and GDC volume fractions and porosity.

Considering the initial TPB density and its long-term stability as primary design criteria, configurations A2 (Ni vol. 29.77%, GDC vol. 45.33%) and A3 (Ni vol. 37.60%, GDC vol. 37.99%) emerge as the most promising, exhibiting high initial TPB density accompanied by relatively low degradation after 2000 hours of aging. A3 additionally demonstrated better nickel percolation compared to A2. Given the MIEC nature of GDC and its role in electrochemical activity and transport, configurations with reduced or even non-percolating Ni content may remain viable depending on the cell design. In this context, B1 (Ni vol. 19.67%, GDC vol. 45.25%), B2 (Ni vol. 25.71%, GDC vol. 39.13%), and C1 (Ni vol. 16.78%, GDC vol. 38.34%) configurations offer favorable trade-offs, exhibiting high initial DPB density, relatively low degradation rates, and stable GDC transport pathways. Among these, the B2 configuration provided the best overall performance whilst prioritizing Ni-related metrics, as it incorporated Ni-percolation along with a relatively high TPB density, and reduced degradation.

The effective elastic properties and average von Mises stress decreased linearly with increasing porosity. For all configurations, the effective elastic properties exhibited a pronounced initial decline corresponding to rapid Ni coarsening in the early stages, followed by a gradual decline or near-constant behavior at longer aging times. The coarsening of the microstructure during aging led to a significant redistribution of local stress fields and substantial changes in global stress conditions resulting from thermal eigenstrains. Microstructures with medium porosity (35%) offered the most balanced mechanical performance by limiting stress localization and critical stress volume fractions during aging. In contrast, anodes with low porosity exhibited increased stress concentrations, while anodes with high porosity showed improved stress tolerance at the expense of lower stiffness and reaction site density values.

Taken together, these findings demonstrate that optimal SOFC anode design requires an integrated electrochemical-mechanical performance consideration based on multiple microstructural descriptors rather than a single-metric optimization. The quantitative results presented here provide guidance for selecting Ni and GDC volume fractions tailored to specific cell designs, while the extracted microstructural parameters serve as necessary inputs for transmission line modeling of Ni-GDC-SOFC anodes for cell performance as a function of microstructural composition, as well as for modeling at the cell and stack levels. A comprehensive investigation of particle size sensitivity and optimization is planned as a natural extension of the present work.

Methods

In this section, we present the comprehensive methodology employed to generate synthetic Ni-GDC SOFC anode microstructures and to model the degradation of microstructural properties pertinent to electrochemical performance and mechanical integrity during aging. The workflow begins with an overview of a synthetic microstructure generation process, including a newly implemented extension to the original structure generator. This is followed by modeling of microstructure coarsening utilizing the phase-field method and formulations of solid mechanics to resolve the stress-strain distribution within the evolving microstructure. Thereafter, we detail the quantification of the 3D Ni-GDC anode microstructure relevant to electrochemical and mechanical performance. Lastly, the validation of the generated synthetic microstructure against an experimental structure and the subsequent generation of fifteen statistically representative synthetic microstructures are discussed.

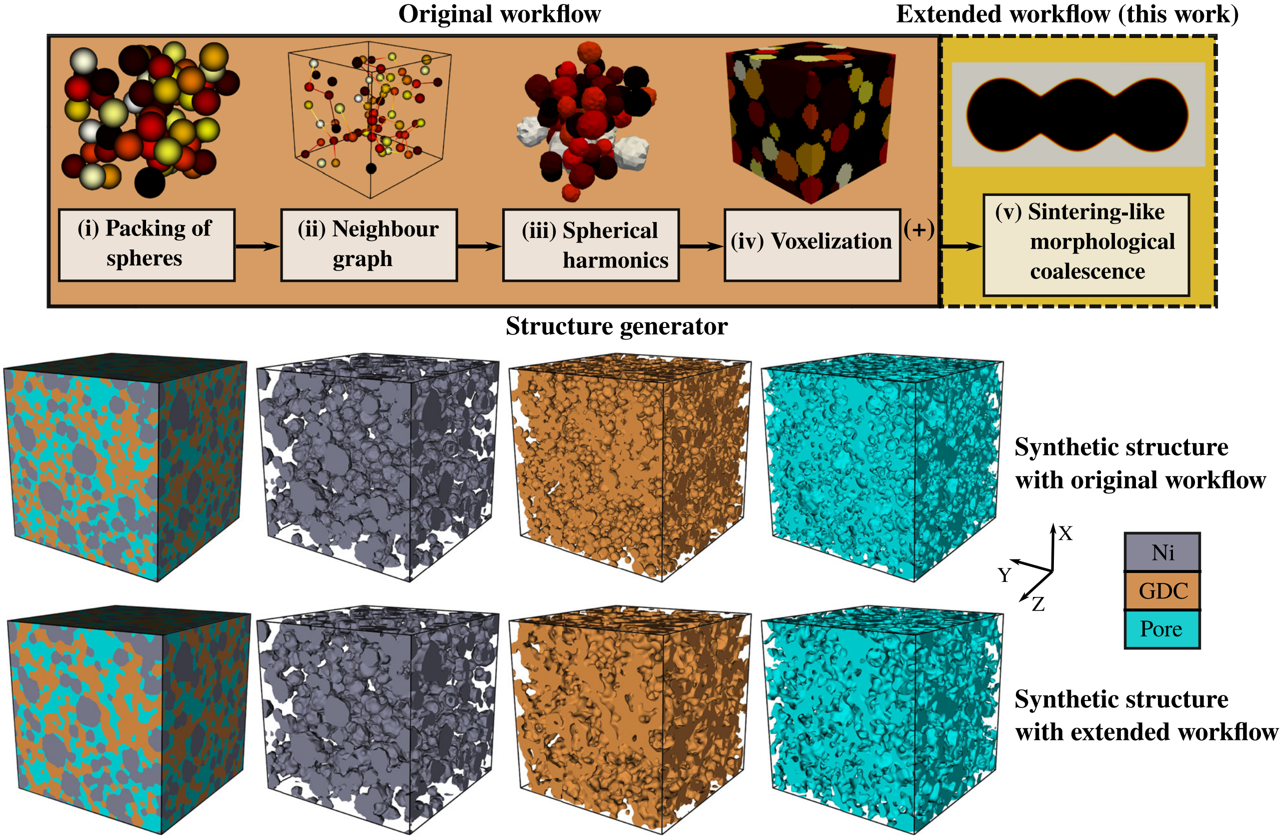

Fig. 11 | Schematic representation of the extended microstructure generation workflow, emphasizing the extended sintering-like morphological coalescence step and resulting enhancements to synthetic solid oxide fuel cells (SOFCs) nickel-gadolinium doped ceria (Ni-GDC) anode microstructures.

Extension of the structure generator for sintering-like morphologies

In the work of Schöller et al.[41], synthetic microstructures were generated in a four-step process as shown in the schematic workflow (original workflow) in Fig. 11: (i) dense packing of hard spheres using a discrete element method, enforcing prescribed particle size distributions for different material phases; (ii) identification of contact points via a neighbor graph connecting all spheres based on a minimum spanning tree (MST); (iii) generation of individual particle geometries using spherical harmonics with specified angular energy spectra, incorporating the previously identified contact points; (iv) The resulting parameterized microstructure was then voxellized and converted into a diffuse-interface representation using a multiphase-field method. Further details on the original framework can be found in ref. 41. Validation of the virtual structure generator was performed by comparison with experimentally reconstructed electrode microstructures in previous work[41]. A comparison of key microstructural descriptors, such as phase volume fractions, specific surface areas, and tortuosities, as well as a qualitative visual comparison, showed that the reported deviations were limited to a few percentage points. The generator relies on several input parameters, such as particle size distributions and angular power spectra; their influence on the resulting morphology is not known a priori. A multi-objective Bayesian optimization was employed to systematically calibrate the generator by minimizing the discrepancy between the morphological metrics of the generated and experimental microstructures across multiple objectives.

Although the original structure generator workflow provides a reasonably close representation of the experimental SOFC anode microstructures and agrees well with several quantitative descriptors, the workflow lacks the ability to generate microstructures more realistic to the experimental structures. In particular, key quantitative metrics such as TPB density and mean particle diameter are not validated against experimental structures. The current work extends the original workflow to further improve synthetic SOFC anode microstructures in comparison to experimental structures. One significant limitation of the original generator is the missing particle coalescence, which results from the sintering stage in the experimental fabrication process. To address this, a sintering-like morphological coalescence step is integrated as an extension of the original workflow. The aim of this extension is not to simulate the physical mechanisms governing sintering, as this would require detailed governing equations, extensive parameterization, and substantial computational resources, as well as time for large 3D domains. Instead, the focus is on efficiently replicating sintering-like morphological features, particularly the formation of sintering neck and particle coalescence, in a computationally tractable manner suitable for synthetic microstructure generation. Figure 11 shows a qualitative comparison between the synthetic microstructures obtained using the original and extended Workflows.

The primary objective of the structure generator workflow extension in this work is to generate synthetic SOFC anode microstructures that are visually and quantitatively representative of the experimental structures across a large set of microstructural descriptors. To achieve sintering-like morphological coalescence in the synthetic structures, a multiphase-field (MPF) method is employed. The MPF method is well established for simulating the evolution of complex microstructures across micro- and mesoscopic length scales. The model utilized in this study is based on the multiphase-field formulation of Steinbach et al.[10] and Nestler et al.[67] and incorporates a targeted modification of the Allen-Cahn equation to simulate sintering-like coalescence while preserving phase volumes. Although the classical Allen-Cahn equation[68] is not inherently volume-conserving, this property can be enforced by means of an extra artificial bulk driving force for volume preservation of specific phases[47]. In addition, an obstacle potential is used together with a corrective term that suppresses the curvature minimization dynamics intrinsic to the Allen-Cahn equation. This curvature minimization behavior, resulting from the Laplace term $\Delta\phi$ in Eq. (7), leads to changes in both phase shape and phase volume. Following the approach proposed by Sun et al.[69], this dynamics can be partially or fully eliminated, enabling controlled morphological coalescence.

In a system with N phases, the microstructure is represented by a set of order parameters $\boldsymbol{\phi} = \{\phi_1, \phi_2, \ldots, \phi_N\}$, whereby each order parameter or phase field variable $\phi_\alpha(\boldsymbol{x}, t)$ represents the presence of phase α at position $\boldsymbol{x}$ and time t. Values $\phi_\alpha = 1$ and $\phi_\alpha = 0$ correspond to the presence or absence of phase α. Diffuse interfaces with finite thickness are employed in place of sharp phase boundaries, where ϕ_α smoothly varies between 0 and 1. The phase field variable ϕ_α can therefore be interpreted as the local volume fraction of phase α. The total free energy $\mathcal{F}$ of a multi-phase heterogeneous material containing N solid phases is represented as the volume integral of the free energy density f over the domain V

$$\mathcal{F}[\boldsymbol{\phi}, \nabla\boldsymbol{\phi}] = \int_V \underbrace{f_{\text{grad}}(\nabla\boldsymbol{\phi}) + f_{\text{pot}}(\boldsymbol{\phi})}_{f_{\text{intf}}(\nabla\boldsymbol{\phi}, \boldsymbol{\phi})} + \underbrace{f(\boldsymbol{\phi}) + g(\boldsymbol{\phi})}_{f_{\text{bulk}}(\boldsymbol{\phi})} \, \mathrm{d}V. \tag{1}$$

Following the notation of Nestler et al.[67], the combined potential f_{pot} and the gradient term f_{grad} together account for the interfacial energy and ensure a diffuse interface with finite thickness. The term $f(\boldsymbol{\phi})$ represents the phase-inherent bulk energy of the phases and acts as the driving force for phase transformation. An additional positive contribution $g(\boldsymbol{\phi})$ enforces the volume preservation of the phases. For more details, interested readers are referred to Nestler et al.[47]. The gradient[10] and potential terms are as follows:

$$f_{\text{grad}}(\nabla\boldsymbol{\phi}) = -\epsilon \sum_{\alpha,\beta>\alpha} \gamma_{\alpha\beta} \nabla\phi_\alpha \cdot \nabla\phi_\beta, \tag{2}$$

$$f_{\text{pot}}(\boldsymbol{\phi}) = \begin{cases} \frac{16}{\epsilon\pi^2} \sum\limits_{\alpha,\beta>\alpha} \gamma_{\alpha\beta}\, \phi_\alpha\phi_\beta + \frac{1}{\epsilon} \sum\limits_{\alpha,\beta>\alpha,\delta>\beta} \gamma_{\alpha\beta\delta}\, \phi_\alpha\phi_\beta\phi_\delta, & \text{if } \boldsymbol{\phi} \in \mathcal{G}, \\ \infty, & \text{otherwise}. \end{cases} \tag{3}$$

Here, $\gamma_{\alpha\beta}$ represents the interfacial energy of the α and β phases, and ϵ controls the diffuse interfacial width. The second term in Eq. (3) prevents the growth of unwanted interfacial contributions at binary interfaces. The order parameter ϕ_α evolution follows an Allen-Cahn type equation driving the system towards minimal energy. The evolution equation reads as follows:

$$\begin{aligned} \frac{\partial\phi_\alpha(\boldsymbol{x},t)}{\partial t} = -\frac{1}{\widetilde{N}\epsilon} \sum_{\beta\neq\alpha}^{\widetilde{N}} \Bigg[M_{\alpha\beta} \Bigg(\frac{\delta f_{\text{intf}}}{\delta\phi_\alpha} - \epsilon\widehat{a}(\phi_\alpha, \nabla\phi_\alpha) \\ - \frac{\delta f_{\text{intf}}}{\delta\phi_\beta} - \epsilon\widehat{a}(\phi_\beta, \nabla\phi_\beta) - \frac{8\sqrt{\phi_\alpha\phi_\beta}}{\pi} \Delta^{\alpha\beta} \Bigg) \Bigg], \end{aligned} \tag{4}$$

where $M_{\alpha\beta}$ represents the mobility, $\widetilde{N}$ refers to the number of locally active phases, and the variational derivative

$$\frac{\delta f}{\delta\phi_\alpha} = \frac{\partial f}{\partial\phi_\alpha} - \nabla \cdot \frac{\partial f}{\partial\nabla\phi_\alpha}. \tag{5}$$

Meanwhile, $\Delta^{\alpha\beta}$ is given as:

$$\Delta^{\alpha\beta} = \left(\frac{\delta}{\delta\phi_\alpha} - \frac{\delta}{\delta\phi_\beta} \right) f_{\text{bulk}}, \tag{6}$$

where f_{bulk} denotes the phase-inherent bulk energy of the phases and an additional positive contribution that enforces volume preservation. As demonstrated by Schoof et al.[48] in the multiphase-field context, the addition of an extra isotropic gradient energy density term, $\epsilon\widehat{a}(\phi_\alpha, \nabla\phi_\alpha)$, to the phase-field evolution is specified as follows:

$$\epsilon\widehat{a}(\phi_\alpha, \nabla\phi_\alpha) = \epsilon\gamma_\alpha^c \left(\Delta\phi_\alpha - |\nabla\phi_\alpha| \nabla \cdot \left(\frac{\nabla\phi_\alpha}{|\nabla\phi_\alpha|} \right) \right). \tag{7}$$

This term enables the calibration of the curvature-driven interface evolution by a surface energy-like parameter γ_α^c, which does not contribute to curvature minimization. The parameter γ_α^c can be understood as a numerical factor for calibrating the strength of the artificially constructed interface. The combined contribution of the interfacial free energy density and this additional isotropic gradient term, as discussed in ref. 48,70, provides a means of controlling the curvature minimization dynamics determined by $\gamma_{\alpha\beta}$. In the present work, these formulations are used as a numerical means of controlling curvature minimization. The extended workflow's ability to generate synthetic microstructures representative of experimental SOFC anode microstructures is validated in this work using an extensive set of quantitative descriptors.

Multiphase-field framework for aging simulations

A simplified modeling approach is followed with the aim of capturing the essential physical mechanisms governing the aging of the Ni-GDC SOFC anode microstructure whilst ensuring computational tractability. In particular, a multiphase-field method based on the grand-potential functional of[20] expanded to include surface self-diffusion[21] is employed to model the coarsening of both the Ni and GDC phases under thermal operating conditions. The porous anode microstructure is represented by three order parameters corresponding to the nickel, GDC, and pore phases. The model assumes mass and volume conservation, isotropic interfacial properties, along with surface and interfacial diffusion as primary mass transport mechanisms. In the current work, each solid phase is treated as homogeneous, and grain boundary effects are not explicitly resolved. Incorporating grain boundary effects and achieving quantitative validation requires reconstructed pristine and aged microstructures with resolved grain boundary or crystallographic orientation information, along with experimentally determined orientation-dependent parameters (e.g., grain boundary energies and diffusion coefficients) under relevant operating conditions, which are currently limited. In our previous work[24], phase-field simulations based on FIB-SEM reconstructed pristine microstructures (without resolved grain boundaries) were quantitatively validated against experimentally aged microstructures (240h and 1100h). For a more detailed discussion, including the scope and limitations of the current modeling framework, the interested reader is referred to the work of Jeela et al.[24]. Coarsening of Ni and GDC is considered to be the predominant degradation mechanism in thermal aging. Accordingly, this study focuses on quantifying the impact of microstructural coarsening on the long-term performance of SOFCs. The model is applicable to Ni-GDC and Ni-YSZ anodes subjected to high-temperature thermal aging in open-circuit conditions. Detailed descriptions of the model formulations, parameters identified by a Bayesian active learning approach and parameterization, as well as the multiphase-field simulation results in comparison to experimentally aged 3D FIB-SEM microstructures after 240 hours and 1100 hours under thermal operating conditions of 900 °C with a gas composition of H_2-50%/H_2O-50% are reported in our previous works[24,25]. Building upon this validated framework, the current work performs large-scale multiphase-field simulations to investigate microstructural evolution over 2000 hours, utilizing a range of initial synthetic microstructures. The temporal evolution of microstructure descriptors relevant to electrochemical performance and mechanical integrity is predicted, enabling the evaluation of distinct anode configurations for optimal initial performance, as well as minimal degradation of performance over long-term operation.

Solid mechanics in PACE3D framework

The effective elastic properties during the aging are determined by load simulations of the aged microstructures within the PACE3D multiphysics framework[26]. A quasi-static solid mechanics formulation is adopted for determining the locally resolved stress and strain fields within the microstructure, assuming negligible body forces and small deformations. Under these assumptions, the momentum balance is given by

$$\nabla \cdot \bar{\boldsymbol{\sigma}} = \mathbf{0},\ \bar{\boldsymbol{\sigma}} = \sum_{\alpha=1}^{N} \phi_\alpha \boldsymbol{\sigma}^\alpha, \tag{8}$$

cf.[71], where $\bar{\boldsymbol{\sigma}}$ refers to the interpolated Cauchy stress calculated from phase-specific stresses $\boldsymbol{\sigma}^\alpha$, and ϕ_α represents the order parameter of the α phase. The infinitesimal strain tensor is interpolated analogously as $\boldsymbol{\varepsilon} = \sum_{\alpha=1}^{N} \phi_\alpha \boldsymbol{\varepsilon}^\alpha$. In accordance with the jump condition approach[72–74], the local phase strain $\boldsymbol{\varepsilon}^\alpha$ is expressed as

$$\boldsymbol{\varepsilon}^\alpha = \boldsymbol{\varepsilon} + \sum_{\delta=1,\delta\neq\alpha}^{N} \phi_\delta \llbracket \boldsymbol{\varepsilon} \rrbracket^{\alpha\delta}, \tag{9}$$

whereby $\llbracket \boldsymbol{\varepsilon} \rrbracket^{\alpha\delta}$ indicates the strain jump over diffuse interfaces between phases α and δ defined by $\llbracket \boldsymbol{\varepsilon} \rrbracket^{\alpha\delta} = \boldsymbol{\varepsilon}^\alpha - \boldsymbol{\varepsilon}^\delta$. The phase-specific strain $\boldsymbol{\varepsilon}^\alpha$ is additively decomposed as $\boldsymbol{\varepsilon}^\alpha = \boldsymbol{\varepsilon}^{\mathrm{el},\alpha} + \boldsymbol{\varepsilon}^{\theta,\alpha}$ with $\boldsymbol{\varepsilon}^{\mathrm{el},\alpha}$ denoting the elastic contribution and $\boldsymbol{\varepsilon}^{\theta,\alpha}$ the thermal contribution. In this regard, $\boldsymbol{\varepsilon}^{\theta,\alpha} = \alpha_\theta^\alpha \Delta\theta \boldsymbol{I}$ is considered, wherein α_θ^α is the isotropic thermal expansion coefficient of the phase α, $\Delta\theta = \theta - \theta_{\mathrm{ref}}^\alpha$ is the temperature difference relative to the reference temperature, and $\boldsymbol{I}$ is the identity tensor of second order.

According to Hooke's law, the corresponding phase-specific stresses in each phase are given by $\boldsymbol{\sigma}^\alpha = \mathbb{C}^\alpha \left[\boldsymbol{\varepsilon}^{\mathrm{el},\alpha}\right] = \mathbb{C}^\alpha \left[\boldsymbol{\varepsilon}^\alpha - \boldsymbol{\varepsilon}^{\theta,\alpha}\right]$, with $\mathbb{C}^\alpha$ indicating the phase-specific stiffness tensor. Under the assumption of isotropic elasticity, the stiffness of phase α is given by $\mathbb{C}^\alpha = 3K^\alpha \mathbb{P}_1 + 2G^\alpha \mathbb{P}_2$, where K^α and G^α denote the compression and shear moduli, respectively. The projection tensors are given by $\mathbb{P}_1 = \frac{1}{3} \boldsymbol{I} \otimes \boldsymbol{I}$ and $\mathbb{P}_2 = \mathbb{I}^S - \mathbb{P}_1$, whereby $\mathbb{I}^S$ refers to the fourth-order symmetric identity. Material properties used for this study are listed in Table 1. As the material properties considered here refer to room temperature conditions, this could result in an overestimation of the predicted absolute values of effective stiffness at the operating temperatures of SOFCs. However, the relative differences in effective stiffness between the microstructures remain unchanged, since all microstructures were evaluated under the same constitutive assumptions.

Microstructure quantification

Microstructural descriptors related to electrochemical performance are discussed below. The geometrical and electrochemically relevant microstructural descriptors of the 3D Ni-GDC SOFC anode, including phase volume fractions, median particle diameter, tortuosity, TPBs, and DPBs, are quantified according to established methods. Collectively, these parameters determine the anode's performance, influencing electrochemical activity and ion, electron, and gas transport significantly, and thus affecting the overall performance of the cell. Particle coarsening is evaluated using continuous particle size distributions, with the median diameter (d_{50}) as the representative measure[75]. Phase tortuosity (τ_α), which describes the complexity of transport pathways, is estimated from the ratio of ideal to effective current, averaged over the three spatial directions to obtain a representative value for the overall transport properties of a phase[76]. The TPB length is calculated using a 3D skeletonization method[77]. The specific surfaces are determined from the phase-field gradients as $A_\alpha = \frac{1}{V} \int_V |\nabla \phi_\alpha| \mathrm{d}V$, whereby each interface ($A_{\alpha-\beta}$) is extracted by solving a set of linear equations. Owing to the mixed conductivity of GDC, the interface between GDC and pores forms the electrocatalytically active surface. All methodologies were implemented in-house within the PACE3D framework and benchmarked against established test cases[19].

Mechanical-related descriptors are described below. The effective elastic properties of the 3D SOFC anode microstructure are determined using numerical homogenization. In this regard, the effective stiffness tensor $\bar{\mathbb{C}}$ is determined using six independent strain-controlled macroscopic load cases. For each load case $\beta = 1, \ldots, 6$, a defined macroscopic strain vector $\bar{\boldsymbol{\varepsilon}}^\beta$ is applied, such that $\mathbf{u} = \varepsilon_0(\mathbf{x}) \in \delta\Omega$ holds true. For example, $\beta = 1$ corresponds to the macroscopic strain $\bar{\boldsymbol{\varepsilon}}^1 = \varepsilon_0\, \mathbf{e}_1 \otimes \mathbf{e}_1$. The solution to the resulting linear elastic boundary value problem yields the local stress field $\boldsymbol{\sigma}^\beta(\mathbf{x})$, from which the volume-averaged macroscopic stress response can be determined as

$$\langle \boldsymbol{\sigma}^\beta \rangle = \frac{1}{V} \int_V \boldsymbol{\sigma}^\beta(\mathbf{x})\, \mathrm{d}V. \tag{10}$$

The macroscopic stress-strain relation from the numerical homogenization scheme is described as follows: $\langle \boldsymbol{\sigma}^\beta \rangle = \bar{\mathbb{C}}\, \bar{\boldsymbol{\varepsilon}}^\beta$. The stiffness contribution for each load case is determined by

$$\underline{\underline{\bar{C}}}^\beta = \frac{\underline{\langle \sigma^\beta \rangle}\, \underline{(\bar{\varepsilon}^\beta)}^T}{\underline{(\bar{\varepsilon}^\beta)}^T \underline{(\bar{\varepsilon}^\beta)}}, \tag{11}$$

where $\underline{\underline{\bar{C}}}$ denotes the matrix representation of the stiffness tensor $\mathbb{C}$ in normed Voigt notation and $\underline{\underline{\bar{C}}}^\beta$ refers to the matrix representation of the βth column of $\underline{\underline{\bar{C}}}$. Each load case results in a column of the effective stiffness tensor. For example, a uniaxial strain $\bar{\boldsymbol{\varepsilon}}^1 = \varepsilon_0\, \mathbf{e}_1 \otimes \mathbf{e}_1$ with the Voigt representation $\underline{\boldsymbol{\varepsilon}}^1 = [\varepsilon_0, 0, 0, 0, 0, 0]^T$ determines the first column of $\bar{\mathbb{C}}$, while shear load cases provide the corresponding shear columns using the standard $\sqrt{2}$ Voigt normalization[78]. Since the mechanical model used for extracting the effective stiffness is fully linear elastic, the homogenized stiffness tensor is independent of the amplitude of ε_0.

The effective stiffness tensor is constructed by superimposing the contributions of all six independent load cases: $\underline{\underline{\bar{C}}} = \sum_{\beta=1}^{6} \underline{\underline{\bar{C}}}^\beta$. The methodology presented in Böhlke and Brüggemann[79] is used to calculate and plot the elastic modulus body. The directional elastic moduli (E_x, E_y, and E_z) can be directly extracted from the elastic modulus body as detailed in ref.79. Beyond the directional moduli, an effective isotropic modulus is obtained by projecting the anisotropic tensor onto its isotropic Voigt and Reuss bounds and combining these using the Hill average[80]. The Voigt estimates of the bulk and shear moduli are then evaluated accordingly

$$K_{Voigt} = \frac{C_{11} + C_{22} + C_{33} + 2(C_{12} + C_{13} + C_{23})}{9}, \tag{12}$$

$$G_{Voigt} = \frac{C_{11} + C_{22} + C_{33} - (C_{12} + C_{13} + C_{23}) + 3(C_{44} + C_{55} + C_{66})}{15}. \tag{13}$$

Whereas the Reuss bounds result from the compliance tensor according to

$$\frac{1}{K_{Reuss}} = S_{11} + S_{22} + S_{33} + 2(S_{12} + S_{13} + S_{23}), \tag{14}$$

$$\frac{1}{G_{Reuss}} = \frac{4}{15}(S_{11} + S_{22} + S_{33} - S_{12} - S_{13} - S_{23}) + \frac{3}{15}(S_{44} + S_{55} + S_{66}). \tag{15}$$

This gives the Hill average values $K_{Hill} = \frac{1}{2}(K_{Voigt} + K_{Reuss})$, $G_{Hill} = \frac{1}{2}(G_{Voigt} + G_{Reuss})$, whereas the effective isotropic modulus of

Table 2 | Input parameters given to the structure generator for creating a synthetic microstructure

Phase	Volume fraction (%)	Mean particle diameter (μm)	Standard deviation (μm)	Angular spectrum amplitude (W nm^{-1})	Dilation iterations
Ni	17.59	0.886	0.352	$10^{-1.8}$	1
GDC	29.21	0.494	0.070	$10^{-2.5}$	1

Table 3 | Comparison of microstructural and mechanical properties: Digital Twin vs. Experimental results

Property	Unit	Phase	Experimental	Synthetic	Relative error (%)
Volume fraction	(%)	Ni	21.92	21.33	−2.69
		GDC	41.57	41.25	−0.77
Mean diameter	(μm)	Ni	0.91	0.91	0
		GDC	0.57	0.57	0
		Pore	0.57	0.55	−3.51
Surface area density	(μm^{-1})	Ni	1.03	1.00	−2.91
		GDC	2.19	1.90	−13.24
		Pore	1.87	2.00	6.95
Mean tortuosity	(−)	Ni	inf	inf	–
		GDC	2.51	2.21	−11.95
		Pore	2.68	3.02	12.69
TPB density	(μm^{-2})	–	1.80	1.95	8.33
DPB density	(μm^{-1})	–	1.51	1.45	−3.97
Elastic moduli	(GPa)	E_{xx}	59.16	62.78	6.11
		E_{yy}	58.47	59.45	1.68
		E_{zz}	63.94	62.52	−2.22
		E_{Hill}	60.40	61.38	1.62

elasticity is given by

$$E_{Hill} = \frac{9K_{Hill}G_{Hill}}{3K_{Hill} + G_{Hill}}. \tag{16}$$

We emphasize that the Voigt-Reuss-Hill estimates give an isotropic projection of the generally anisotropic effective stiffness tensor and should therefore solely be used as scalar measures for comparing the overall stiffness evolution across different aging states.

Synthetic microstructure generation and experimental validation

The performance of the extended structure generator in replicating experimental microstructural features of the SOFC anode was evaluated by generating a synthetic SOFC anode microstructure utilizing particle size distributions and phase volume fractions derived from a 3D FIB-SEM reconstructed experimental microstructure[25] as input for the generator. The generated structure was subsequently validated against the experimental reference through a combination of visual assessment and comprehensive quantitative metrics. Since the multi-stage structure generator workflow depends on several input parameters, such as phase volume fractions, particle size distributions, angular power spectra, and dilation factors, whose effects on the resulting morphology are not known a priori, a multi-objective Bayesian optimization (BO) approach was used for systematic calibration. A total of 200 trials were performed to minimize the global deviation from an experimental reference microstructure, with emphasis on key metrics such as phase volume fractions, tortuosities, and specific surface densities of the Ni, GDC, and pore phases. The resulting database was analyzed to refine the parameter search space and identify suitable fixed input parameters.

Following the BO calibration, a limited number of manual tuning iterations were performed to adjust the simulation time and tuning parameters for curvature minimization that control the sintering-like morphological evolution, aiming to achieve TPB densities closer to the experimental values as well as to achieve particle coalescence in an efficient manner. The model parameters were determined through an iterative manual tuning procedure, in which the curvature control parameter and the interfacial energy configurations were adjusted to achieve closer agreement between simulated and experimental microstructural descriptors (e.g., TPB density, DPB density, and surface area densities). This was achieved by controlling the curvature-driven evolution to obtain realistic morphologies within a limited number of iterations, followed by a minor refinement of the interfacial energies to enhance the agreement with the target values. Without this sintering-like morphological step, the generated structures exhibit much higher TPB densities than the experimental reference structure, as the generated structures consist of isolated, nearly spherical particles resembling green body configurations. Since the primary objective of the current work is to investigate the influence of initial microstructure configurations on degradation behavior, a total of 15 synthetic microstructures with predetermined volume fractions and particle sizes need to be generated. All other generator parameters are defined based on a combination of BO calibration and manual fine-tuning to ensure consistency across all generated structures, without necessitating repeated experimental validation for each structure. The optimization and validation approach thus establishes a robust set of parameters to be employed consistently across the generation of all synthetic microstructures. The Bayesian optimization was performed on a reduced but statistically representative domain, keeping the experimental voxel resolution[25], to reduce computational effort. For a more detailed description of the original structure generator, parameter sensitivities, and BO framework, the reader is referred to Schöller et al.[41]. The optimized input parameters given to the structure generator for creating a synthetic microstructure are summarized in Table 2. The mean particle diameter and standard deviation listed in Table 2 define the lognormal particle size distribution employed as input for the synthetic structure generation procedure to generate particle size distributions from a given distribution.

The extended workflow incorporates a sintering-like morphological coalescence step based on a modified Allen-Cahn phase-field equation that preserves the volume[47], as well as a correction term controlling curvature minimization[48], as described in Extension of the structure generator for sintering-like morphologies section. All parameters are expressed in a consistent arbitrary unit system. To accelerate morphological evolution, equal interfacial mobilities were assigned across all phase pairs, with $M_{NiPore} = M_{NiGDC} = M_{GDCPore} = 1\ u_l^4/\left(u_E u_t\right)$. The interfacial energies were set to $(\gamma_{\mathrm{NiGDC}}, \gamma_{\mathrm{NiPore}}, \gamma_{\mathrm{GDCPore}}) = (1.43,\ 1.2,\ 2.43)$, while the curvature control parameter was chosen as $\gamma_\alpha^c = 9u_E/u_l^2$. A higher-order term $\gamma_{\alpha\beta\delta} = 50u_E/u_l^2$ was included to suppress the formation of spurious phase formation. The simulations were performed using an interfacial width parameter ϵ as 2.0 u_l, number of time steps as 100, and a total simulation time of 2.5 u_t. It is emphasized that this morphological evolution does not represent a physical sintering process. Instead, the phase-field simulations are employed as a numerical tool to generate sintering-like morphologies through particle coalescence rapidly. Accordingly, the simulation time represents a pseudo-time, and the parameters for mobility and surface energy are treated as numerical controls governing the rate and extent of morphological evolution.

The representativeness of the synthetic microstructure was evaluated by systematically comparing a comprehensive set of geometric, statistical,

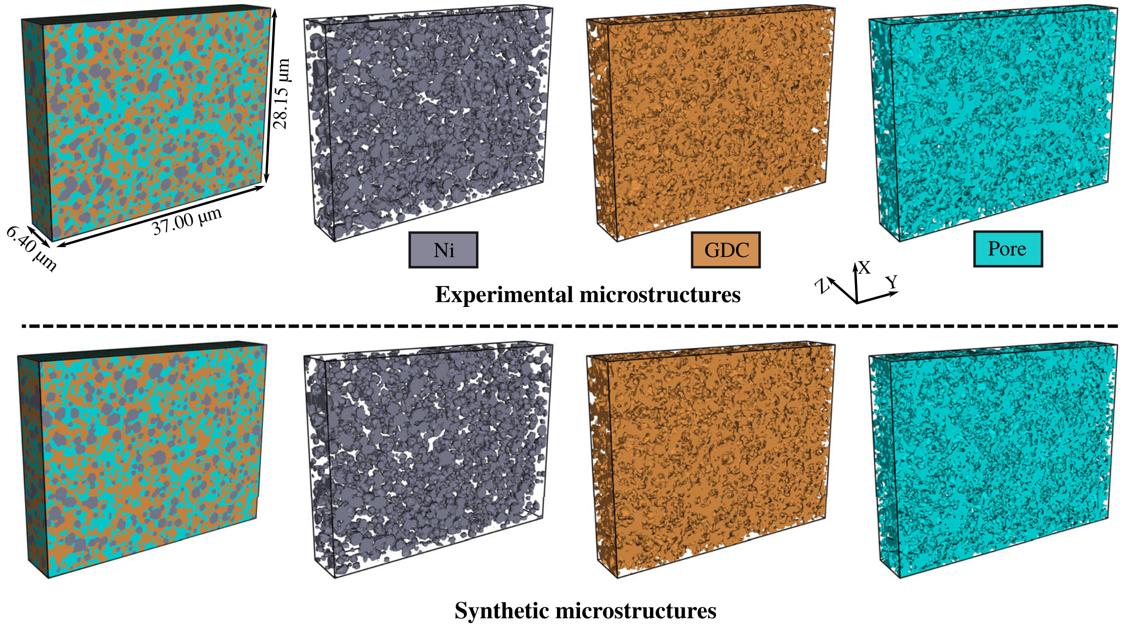

Fig. 12 | Comparison of the Focused Ion Beam Scanning Electron Microscopy (FIB-SEM) reconstructed 3D solid oxide fuel cells (SOFCs) anode microstructure[25] and the individual phase morphologies with a digital twin created by a structure generator.

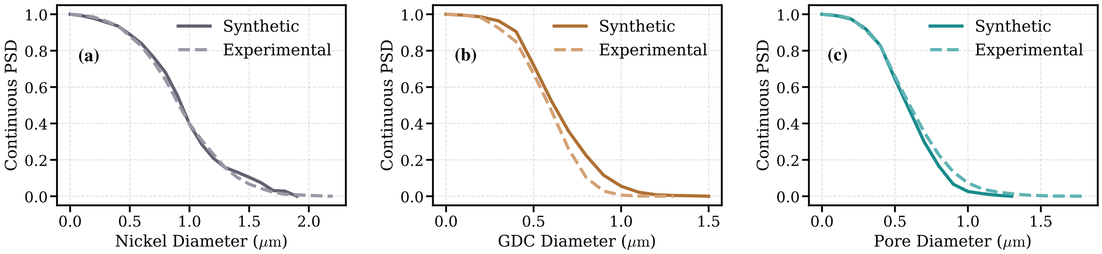

Fig. 13 | Comparison of particle size distributions of synthetic and reconstructed microstructures. Continuous particle size distributions (PSD) for the synthetic microstructure and the Focused Ion Beam Scanning Electron Microscopy (FIB-SEM) reconstructed anode for **a** nickel phase, **b** gadolinium-doped ceria (GDC) phase, and **c** pore phase.

and microstructural descriptors, relevant to both electrochemical performance and mechanical behavior, with an experimental reference structure (Table 3). The employed experimental 3D microstructure was reconstructed from Ni-GDC SOFC anode samples produced at Forschungszentrum Jülich and FIB-SEM tomography at KIT[9]. The statistical representativeness of the experimental domain and its subvolumes was demonstrated in our previous work[25]. The 3D experimental and synthetic microstructures are shown in Fig. 12. A visual inspection reveals a high degree of morphological resemblance at both the electrode and phase levels, including particle shapes, phase connectivity, and spatial distribution. A quantitative assessment, as shown in the Table 3, validates this agreement across an extensive set of 17 quantitative metrics. Most relative errors remain below 5%, with larger discrepancies of 11 to 13% observed for GDC surface area density and the tortuosities. The generator precisely replicates the phase volume fractions and particle sizes of Ni, GDC, and pores, while showing high agreement in the specific surface areas for Ni and pore phases; the GDC surface area shows a higher underestimation of around 13%. TPB and DPB densities, important descriptors for electrochemical activity, are reproduced with errors of about 8% and 4%, respectively. The inclusion of a sintering-like coalescence step proves essential in achieving TPB values closer to those observed in experiments. The tortuosity values show larger deviations of about 12% for GDC and pore phases. These values are highly sensitive to local microstructural changes. The tortuosity of nickel is not reported, as the Ni phase is not percolating in both experimental and synthetic structures. The directional and effective elastic moduli are also well captured and largely agree with the experimental values.

In order to quantify the overall accuracy of the synthetic microstructure, a global error metric was calculated, defined as the mean absolute percentage error (MAPE) in all metrics considered, which yields a value of 4.92%, calculated from 16 parameters. One parameter with an infinite reference value was excluded, as the percentage error is undefined in this case. This single scalar metric demonstrates the generator's ability to accurately reproduce across a wide range of geometric, transport-related, and mechanical properties. The strong agreement in both morphology and quantitative descriptors confirms the synthetic structure as a digital twin of the real SOFC anode and enables subsequent sensitivity analyses, correlations between microstructure and properties, to guide optimization of the electrodes. This work employs the continuous particle size distribution method of Münch and Holzer[75], which is particularly useful for porous networks as it avoids artificial segmentation into discrete particles. The method determines the fraction of the phase volume that can be occupied by overlapping spheres of a certain diameter and, in principle, results in a complementary cumulative distribution that decreases monotonically from unity to zero. For the validation of the generated synthetic microstructure, the continuous particle size distributions of the nickel, GDC, and pore phases are compared with those obtained from 3D FIB-SEM reconstruction (Fig. 13). The close agreement across all phases, as shown in Fig. 13, further supports the validation of the generated structure in comparison to the

Table 4 | Evaluation of statistical variations in microstructural properties across 10 synthetic structures (S1 to S10 samples) generated independently under identical conditions from the structure generator

Property	S1	S2	S3	S4	S5	S6	S7	S8	S9	S10	Mean	Standard deviation	Coefficient of Variation (%)
TPB density (μm^{-2})	1.90	1.92	1.88	1.86	1.96	1.86	1.86	1.87	1.95	1.89	1.89	0.03528	1.86
DPB density (μm^{-1})	1.46	1.46	1.48	1.44	1.43	1.47	1.46	1.47	1.45	1.45	1.46	0.01418	0.97
Ni SA density (μm^{-1})	0.95	0.96	0.95	0.96	0.99	0.95	0.96	0.95	0.98	0.97	0.96	0.01327	1.38
GDC SA density (μm^{-1})	1.90	1.89	1.90	1.87	1.89	1.89	1.90	1.89	1.89	1.89	1.89	0.00831	0.44
Pore SA density (μm^{-1})	1.98	1.98	2.01	1.97	1.95	1.99	1.98	1.99	2.00	1.99	1.98	0.01562	0.79
GDC Mean tortuosity (−)	2.19	2.20	2.17	2.26	2.26	2.22	2.18	2.19	2.18	2.21	2.21	0.03040	1.38
Pore Mean tortuosity (−)	2.93	3.13	2.86	3.01	3.12	2.97	3.13	2.98	3.10	2.99	3.02	0.08908	2.95
Ni Mean diameter (μm)	0.93	0.94	0.94	0.88	0.91	0.93	0.95	0.90	0.93	0.94	0.92	0.02062	2.23
GDC Mean diameter (μm)	0.57	0.57	0.58	0.59	0.58	0.58	0.58	0.58	0.58	0.57	0.58	0.00600	1.04
Pore Mean diameter (μm)	0.56	0.56	0.55	0.55	0.56	0.55	0.56	0.56	0.56	0.56	0.56	0.00458	0.82
E_{xx} (GPa)	59.57	61.04	61.81	59.72	61.86	60.51	60.18	59.48	61.34	61.38	60.69	0.87160	1.44
E_{yy} (GPa)	60.69	61.14	59.35	60.11	59.97	61.40	60.50	59.51	59.99	59.75	60.24	0.64370	1.07
E_{zz} (GPa))	60.59	61.74	59.71	61.80	61.17	60.93	60.61	61.04	61.92	61.03	61.05	0.63450	1.04
E_{Hill} (GPa)	60.18	61.26	60.00	60.07	60.72	60.78	60.39	60.00	60.83	60.38	60.46	0.40150	0.66

Table 5 | Microstructural parameters of the generated synthetic structures

Synthetic structures	Pore vol. frac. (%)	Ni		GDC		Ni Mean dia. (μm)		GDC Mean dia. (μm)	
		Target (solid vol. %)	Synthetic (vol. %)	Target (solid vol. %)	Synthetic (vol. %)	Target	Synthetic	Target	Synthetic
A1	**25**	**30**	22.51	**70**	52.57	**0.75**	0.757	**0.50**	0.508
A2		**40**	29.77	**60**	45.33		0.737		0.495
A3		**50**	37.60	**50**	37.99		0.740		0.493
A4		**60**	45.00	**40**	30.52		0.749		0.514
A5		**70**	52.71	**30**	22.87		0.755		0.499
B1	**35**	**30**	19.67	**70**	45.28	**0.75**	0.748	**0.50**	0.502
B2		**40**	25.71	**60**	39.13		0.761		0.498
B3		**50**	32.66	**50**	32.37		0.756		0.502
B4		**60**	38.91	**40**	26.10		0.758		0.502
B5		**70**	45.26	**30**	19.34		0.762		0.506
C1	**45**	**30**	16.78	**70**	38.34	**0.75**	0.753	**0.50**	0.497
C2		**40**	22.08	**60**	32.94		0.742		0.510
C3		**50**	27.58	**50**	27.34		0.750		0.504
C4		**60**	32.85	**40**	21.96		0.753		0.497
C5		**70**	38.60	**30**	16.50		0.748		0.499

The bold values denote the target (reference) parameters used in the design of the fifteen synthetic microstructures, while the remaining values represent the corresponding realized parameters obtained from the generated structures.

experimental microstructure. Furthermore, a statistical analysis of 10 independently generated microstructures under identical conditions (as in the validation case) was performed, and the resulting variability in key microstructural properties is summarized in Table 4. The low variance observed across a wide range of properties, with coefficients of variation of about 1% for the majority of properties and 2–3% for two other properties, confirms the robustness and reproducibility of the structure generation method. This further demonstrates the reliability of the comparisons presented in this work.

Generation of synthetic structures for aging simulations

The influence of initial phase volume fractions on microstructural attributes that govern electrochemical performance and mechanical behavior initially and during aging was investigated by generating a series of synthetic microstructures through variation of phase volume fractions. Fifteen synthetic microstructures were created by varying the volume fractions of Ni, GDC, and pore phases while maintaining constant particle sizes. The targeted parameters for analysis and their values in the generated synthetic structures are summarized in Table 5. Three pore volume fractions were considered: 25% (group A), 35% (group B), and 45% (group C). Within each group, five configurations were generated by varying the Ni/GDC solid phase ratio in 10% increments from 30/70 to 70/30. These parameter ranges comprise widely reported experimental and investigated compositions and enable a systematic evaluation of the effects resulting from the volume fractions of the three phases. To isolate the influence of particle sizes, the average particle sizes of Ni and GDC were kept constant in all configurations. Average particle diameters of 0.75 μm for Ni and 0.5 μm for GDC were chosen, corresponding largely to the experimental values for conventional screen-printed anodes. The resulting particle sizes in all generated microstructures remained close to these target values, as shown in Table 5.

Some representative examples of generated synthetic microstructures are shown in the first row of Fig. 3. The statistical representativeness of the microstructures is ensured by the appropriate domain size, voxel resolution, and number of particles. All synthetic microstructures comprise a cubic domain of $10^3 \mu m^3$ and a voxel size of 35 nm, providing sufficient resolution while maintaining computational tractability for long-term aging simulations. The volume of the domain is well above the representative volume element (RVE) threshold of 10^3 particles, where most properties converge to stable values, as found by Joos et al.[81]. In our previous work[25], statistical error analysis of a FIB-SEM reconstructed domain (9.4 x 12.4 x 6.4 μm^3) demonstrated low variability in microstructural properties, with coefficients of variation (CV) ranging from 1-5% (mean CV of about 3%), confirming negligible spatial heterogeneity. In the current work, the simulation domain of 10.0 x 10.0 x 10.0 μm^3 with a total volume of 1000 μm^3 is comparable to and slightly larger than the previously validated representative volume, ensuring statistical representativeness. Accordingly, any microstructural inhomogeneities are expected to be minimal, with no significant influence on the computed properties. Structure generator enables direct and flexible control over phase volume fractions and particle sizes. By modifying the parameters of the particle size distribution, microstructures with finer or coarser particle sizes can be systematically generated. Comprehensive investigation of particle size sensitivity and optimization, however, is beyond the scope of the current study and is planned for future work.

Data availability

The datasets generated and/or analyzed during the current study are not publicly available due to their use in ongoing research; however, all relevant data are provided within the article, but are available from the corresponding author on reasonable request. The datasets generated and analyzed during the current study were produced using the proprietary Pace3D simulation framework developed at the Karlsruhe University of Applied Sciences [[27,82]], the open-source Lammps molecular dynamics package [[83]], and the open-source Optuna optimization framework [[84]]. Due to licensing restrictions, the Pace3D source code cannot be made publicly available. However, licenses can be obtained upon request.

Code availability

The datasets generated and analyzed during the current study were produced using the proprietary PACE3D simulation framework developed at the Karlsruhe University of Applied Sciences[27,82], the open-source LAMMPS molecular dynamics package[83], and the open-source OPTUNA optimization framework[84]. Due to licensing restrictions, the PACE3D source code cannot be made publicly available. However, licenses can be obtained upon request.

Received: 12 March 2026; Accepted: 7 May 2026;

References

1. Yamamoto, K., Qiu, N. & Ohara, S. In situ fabrication of high-performance Ni-GDC-nanocube core-shell anode for low-temperature solid-oxide fuel cells. *Sci. Rep.* **5**, 17433 (2015).
2. Jaiswal, N. et al. A brief review on ceria based solid electrolytes for solid oxide fuel cells. *J. Alloy. Compd.* **781**, 984–1005 (2019).
3. Zhang, J., Lenser, C., Menzler, N. H. & Guillon, O. Comparison of solid oxide fuel cell (SOFC) electrolyte materials for operation at 500 c. *Solid State Ion.* **344**, 115138 (2020).
4. Eguchi, K., Setoguchi, T., Inoue, T. & Arai, H. Electrical properties of ceria-based oxides and their application to solid oxide fuel cells. *Solid State Ion.* **52**, 165–172 (1992).
5. Zekri, A., Knipper, M., Parisi, J. & Plaggenborg, T. Microstructure degradation of Ni/Cgo anodes for solid oxide fuel cells after long operation time using 3D reconstructions by fib tomography. *Phys. Chem. Chem. Phys.* **19**, 13767–13777 (2017).
6. Fang, Q., Frey, C. E., Menzler, N. H. & Blum, L. Electrochemical performance and preliminary post-mortem analysis of a solid oxide cell stack with 20,000 h of operation. *J. Electrochem. Soc.* **165**, F38 (2018).
7. Trini, M. et al. Comparison of microstructural evolution of fuel electrodes in solid oxide fuel cells and electrolysis cells. *J. Power Sources* **450**, 227599 (2020).
8. Holzer, L. et al. Microstructure degradation of cermet anodes for solid oxide fuel cells: Quantification of nickel grain growth in dry and in humid atmospheres. *J. Power Sources* **196**, 1279–1294 (2011).
9. Liu, Y. et al. Microstructural changes in nickel-ceria fuel electrodes at elevated temperature. *Fuel Cells* **23**, 430–441 (2023).
10. Steinbach, I. & Pezzolla, F. A generalized field method for multiphase transformations using interface fields. *Phys. D.* **134**, 385–393 (1999).
11. Nestler, B. & Choudhury, A. Phase-field modeling of multi-component systems. *Curr. Opin. Solid State Mater. Sci.* **15**, 93–105 (2011).
12. Prahs, A., Schneider, D. & Nestler, B. A continuum thermodynamic approach to the phase-field method: the order parameter as internal state variable. *Contin. Mech. Thermodyn.* **37**, 55 (2025).
13. Prahs, A., Elmoghazy, A., Schneider, D. & Nestler, B. The multiphase-field method based on internal state variables. *Contin. Mech. Thermodyn.* **38**, 47 (2026).
14. Chen, H.Y. et al. Simulation of coarsening in three-phase solid oxide fuel cell anodes. *J. Power Sources* **196**, 1333–1337 (2011).
15. Li, Q., Liang, L., Gerdes, K. & Chen, L.-Q. Phase-field modeling of three-phase electrode microstructures in solid oxide fuel cells. *Appl. Phys. Lett.* **101**, 033909 (2012).
16. Jiao, Z. & Shikazono, N. Simulation of the reduction process of solid oxide fuel cell composite anode based on phase field method. *J. Power Sources* **305**, 10–16 (2016).
17. Wang, Y. et al. Morphology and performance evolution of anode microstructure in solid oxide fuel cell: A model-based quantitative analysis. *Appl. Energy Combust. Sci.* **5**, 100016 (2021).
18. Yang, S. et al. Ni coarsening in ni-yttria stabilized zirconia electrodes: Three-dimensional quantitative phase-field simulations supported by ex-situ ptychographic nano-tomography. *Acta Mater.* **246**, 118708 (2023).
19. Hoffrogge, P. W. et al. Performance estimation by multiphase-field simulations and transmission-line modeling of nickel coarsening in fib-sem reconstructed Ni-YSZ SOFC anodes i: Influence of wetting angle. *J. Power Sources* **570**, 233031 (2023).
20. Choudhury, A. & Nestler, B. Grand-potential formulation for multicomponent phase transformations combined with thin-interface asymptotics of the double-obstacle potential. *Phys. Rev. E* **85**, 021602 (2012).
21. Hoffrogge, P. W. et al. Multiphase-field model for surface diffusion and attachment kinetics in the grand-potential framework. *Phys. Rev. E* **103**, 033307 (2021).
22. Sun, M. et al. Microstructure evolution and performance evaluation of nickel/gadolinium-doped ceria fuel electrode for solid oxide fuel cell investigated by integrated meso-scale modeling. https://doi.org/10.2139/ssrn.5037533 (2024).
23. Chang, Z., Bao, C., Lu, X. & Mi, S. Numerical reconstruction and evolution of nickel and gadolinium doped ceria anode microstructure based on phase-field method. *Int. J. Hydrog. Energy* **172**, 151141 (2025).
24. Jeela, R. et al. Multiphase-field simulation studies of coarsening in Ni-GDC SOFC anode microstructures and the effect of interfacial energies. *ACS Appl. Energy Mater.* **8**, 17670–17687 (2025).
25. Jeela, R. et al. Enhancing solid oxide fuel cells development through Bayesian active learning. *Adv. Energy Mater.* **15**, 2501216 (2025).
26. Pace3D (Phase-field Algorithms for Computational Engineering in 3D) (KIT). https://www.iam.kit.edu/mms/pace3d.php (2026)
27. Hötzer, J. et al. The parallel multi-physics phase-field framework pace3d. *J. Comput. Sci.* **26**, 1–12 (2018).

28. Seiz, M. et al. Phase-field simulations with the grand potential approach (2021).
29. Selcuk, A. & Atkinson, A. Elastic properties of ceramic oxides used in solid oxide fuel cells (SOFC). *J. Eur. Ceram. Soc.* **17**, 1523–1532 (1997).
30. Radovic, M. & Lara-Curzio, E. Mechanical properties of tape cast nickel-based anode materials for solid oxide fuel cells before and after reduction in hydrogen. *Acta Mater.* **52**, 5747–5756 (2004).
31. Nakajo, A. et al. Compilation of mechanical properties for the structural analysis of solid oxide fuel cell stacks. constitutive materials of anode-supported cells. *Ceram. Int.* **38**, 3907–3927 (2012).
32. Basu, R., Kumar, S. S., Mukhopadhyay, A. K. & Maiti, H. S. Improvement in mechanical properties of anode-supported planar SOFC. *ECS Trans.* **7**, 533–541 (2007).
33. Liu, X. et al. Correlation between microstructures and macroscopic properties of nickel/yttria-stabilized zirconia (Ni-YSZ) anodes: Meso-scale modeling and deep learning with convolutional neural networks. *Energy AI* **7**, 100122 (2022).
34. Elmoghazy, A. et al. Investigations on the microstructural degradation and mechanical response of Ni-CGO anodes using phase-field method and stochastic modeling. https://doi.org/10.2139/ssrn.6749426 (2026).
35. Kim, Y. J. & Lee, M. C. Numerical investigation of flow/heat transfer and structural stress in a planar solid oxide fuel cell. *Int. J. Hydrog. Energy* **42**, 18504–18513 (2017).
36. Yeong, C. L. & Torquato, S. Reconstructing random media. *Phys. Rev. E* **57**, 495 (1998).
37. Westhoff, D., Manke, I. & Schmidt, V. Generation of virtual lithium-ion battery electrode microstructures based on spatial stochastic modeling. *Comput. Mater. Sci.* **151**, 53–64 (2018).
38. Gayon-Lombardo, A., Mosser, L., Brandon, N. P. & Cooper, S. J. Pores for thought: generative adversarial networks for stochastic reconstruction of 3d multi-phase electrode microstructures with periodic boundaries. *npj Comput. Mater.* **6**, 82 (2020).
39. Abbaspour, A., Luo, J.-L. & Nandakumar, K. Three-dimensional random resistor-network model for solid oxide fuel cell composite electrodes. *Electrochim. Acta* **55**, 3944–3950 (2010).
40. Zheng, K. & Ni, M. Reconstruction of solid oxide fuel cell electrode microstructure and analysis of its effective conductivity. *Sci. Bull.* **61**, 78–85 (2016).
41. Schöller, L., Wehner, L., Schneider, D., Schwaiger, R. & Nestler, B. Virtual design of multilayered SOFC microstructures based on particlepacking and spherical harmonics. *Model. Simul. Mater. Sci. Eng.* https://doi.org/10.1088/1361-651X/ae7138 (2026).
42. Feinauer, J. et al. Stochastic 3d modeling of the microstructure of lithium-ion battery anodes via Gaussian random fields on the sphere. *Comput. Mater. Sci.* **109**, 137–146 (2015).
43. Timurkutluk, B., Ciflik, Y., Altan, T. & Genc, O. Synthetical designing of solid oxide fuel cell electrodes: Effect of particle size and volume fraction. *Int. J. Hydrog. Energy* **47**, 31446–31458 (2022).
44. Prioux, M. et al. Numerical microstructural optimization for the hydrogen electrode of solid oxide cells. *Fuel Cells* **23**, 408–419 (2023).
45. Muetter, F. et al. Artificial intelligence for solid oxide fuel cells: Combining automated high accuracy artificial neural network model generation and genetic algorithm for time-efficient performance prediction and optimization. *Energy Convers. Manag.* **291**, 117263 (2023).
46. Peng, J., Zhao, D., Xu, Y., Wu, X. & Li, X. Comprehensive analysis of solid oxide fuel cell performance degradation mechanism, prediction, and optimization studies. *Energies* **16**, 788 (2023).
47. Nestler, B., Wendler, F., Selzer, M., Stinner, B. & Garcke, H. Phase-field model for multiphase systems with preserved volume fractions. *Phys. Rev. E* **78**, 011604 (2008).
48. Schoof, E. et al. Multiphase-field modeling of martensitic phase transformation in a dual-phase microstructure. *Int. J. Solids Struct.* **134**, 181–194 (2018).
49. Chen, D., Lin, Z., Zhu, H. & Kee, R. J. Percolation theory to predict effective properties of solid oxide fuel-cell composite electrodes. *J. Power Sources* **191**, 240–252 (2009).
50. Kenney, B., Valdmanis, M., Baker, C., Pharoah, J. & Karan, K. Computation of tpb length, surface area and pore size from numerical reconstruction of composite solid oxide fuel cell electrodes. *J. Power Sources* **189**, 1051–1059 (2009).
51. Bertei, A. & Nicolella, C. Percolation theory in SOFC composite electrodes: Effects of porosity and particle size distribution on effective properties. *J. Power Sources* **196**, 9429–9436 (2011).
52. Wang, S., Kobayashi, T., Dokiya, M. & Hashimoto, T. Electrical and ionic conductivity of Gd-doped ceria. *J. Electrochem. Soc.* **147**, 3606 (2000).
53. Gibson, L. J. & Ashby, M. F.Cellular Solids: Structure and Properties Cambridge University Press, (1997).
54. Pihlatie, M., Kaiser, A. & Mogensen, M. Mechanical properties of nio/ni–ysz composites depending on temperature, porosity and redox cycling. *J. Eur. Ceram. Soc.* **29**, 1657–1664 (2009).
55. Pabst, W., Gregorová, E. & Tichá, G. Elasticity of porous ceramics-a critical study of modulus- porosity relations. *J. Eur. Ceram. Soc.* **26**, 1085–1097 (2006).
56. Kishimoto, M., Lomberg, M., Ruiz-Trejo, E. & Brandon, N. P. Numerical modeling of nickel-infiltrated gadolinium-doped ceria electrodes reconstructed with focused ion beam tomography. *Electrochim. Acta* **190**, 178–185 (2016).
57. Xiang, Y., Da, Y., Shikazono, N. & Jiao, Z. Quantitative study on solid oxide fuel cell anode microstructure stability based on 3d microstructure reconstructions. *J. Power Sources* **477**, 228653 (2020).
58. Vivet, N. et al. Effect of Ni content in SOFC Ni-ysz cermets: A three-dimensional study by fib-sem tomography. *J. Power Sources* **196**, 9989–9997 (2011).
59. Hoffrogge, P. W.Understanding degradation phenomena in solid-oxide fuel-cell anodes by phase-field modeling and analytics, KIT Scientific Publishing, (2024).
60. Miyawaki, K., Kishimoto, M., Iwai, H., Saito, M. & Yoshida, H. Comprehensive understanding of the active thickness in solid oxide fuel cell anodes using experimental, numerical and semi-analytical approach. *J. Power Sources* **267**, 503–514 (2014).
61. Chueh, W. C., Hao, Y., Jung, W. & Haile, S. M. High electrochemical activity of the oxide phase in model ceria–pt and ceria–ni composite anodes. *Nat. Mater.* **11**, 155–161 (2012).
62. Nakamura, T. et al. Determination of the reaction zone in gadolinia-doped ceria anode for solid oxide fuel cell. *J. Electrochem. Soc.* **155**, B1244–B1250 (2008).
63. Nakamura, T. et al. Electrochemical behaviors of mixed conducting oxide anodes for solid oxide fuel cell. *J. Electrochem. Soc.* **155**, B563–B569 (2008).
64. Brus, G., Iwai, H. & Szmyd, J. S. An anisotropic microstructure evolution in a solid oxide fuel cell anode. *Nanoscale Res. Lett.* **15**, 3 (2020).
65. Xiang, Y., Da, Y., Zhong, Z., Shikazono, N. & Jiao, Z. Thermo-mechanical stress analyses of solid oxide fuel cell anode based on three-dimensional microstructure reconstruction. *Int. J. Hydrog. Energy* **45**, 19791–19800 (2020).
66. Celik, S., Ibrahimoglu, B., Toros, S. & Mat, M. D. Three dimensional stress analysis of solid oxide fuel cell anode micro structure. *Int. J. Hydrog. Energy* **39**, 19119–19131 (2014).
67. Nestler, B., Garcke, H. & Stinner, B. Multicomponent alloy solidification: phase-field modeling and simulations. *Phys. Rev. E* **71**, 041609 (2005).
68. Allen, S. M. & Cahn, J. W. A microscopic theory for antiphase boundary motion and its application to antiphase domain coarsening. *Acta Metall.* **27**, 1085–1095 (1979).
69. Sun, Y. & Beckermann, C. Sharp interface tracking using the phase-field equation. *J. Comput. Phys.* **220**, 626–653 (2007).

70. Chen, C., Lin, H. & Lan, C. Phase field modeling with large interface thickness and undercooling. *J. Cryst. Growth* **385**, 121–126 (2014).
71. Schneider, D. et al. Phase-field elasticity model based on mechanical jump conditions. *Comput. Mech.* **55**, 887–901 (2015).
72. Durga, A., Wollants, P. & Moelans, N. Evaluation of interfacial excess contributions in different phase-field models for elastically inhomogeneous systems. *Model. Simul. Mater. Sci. Eng.* **21**, 055018 (2013).
73. Mosler, J., Shchyglo, O. & Hojjat, H. M. A novel homogenization method for phase field approaches based on partial rank-one relaxation. *J. Mech. Phys. Solids* **68**, 251–266 (2014).
74. Schneider, D. et al. On the stress calculation within phase-field approaches: a model for finite deformations. *Comput. Mech.* **60**, 203–217 (2017).
75. Münch, B. & Holzer, L. Contradicting geometrical concepts in pore size analysis attained with electron microscopy and mercury intrusion. *J. Am. Ceram. Soc.* **91**, 4059–4067 (2008).
76. Joos, J., Carraro, T., Weber, A. & Ivers-Tiffée, E. Reconstruction of porous electrodes by fib/sem for detailed microstructure modeling. *J. Power Sources* **196**, 7302–7307 (2011).
77. Palágyi, K. & Kuba, A. A 3d 6-subiteration thinning algorithm for extracting medial lines. *Pattern Recognit. Lett.* **19**, 613–627 (1998).
78. Bertram, A. Elasticity and plasticity of large deformations: including gradient materials. Springer Nature, (2021).
79. Böhlke, T. & Brüggemann, C. Graphical representation of the generalized Hooke's law. *Tech. Mech.* **21**, 145–158 (2001).
80. Hill, R. The elastic behaviour of a crystalline aggregate. *Proc. Phys. Soc. A* **65**, 349 (1952).
81. Joos, J. Microstructural characterisation, modelling and simulation of solid oxide fuel cell cathodes, vol. 30 KIT Scientific Publishing, (2017).
82. Institute of Digital Materials Science (IDM), Karlsruhe University of Applied Sciences. Pace3D – A Parallel Phase-Field Framework. https://www.h-ka.de/en/idm/profile/pace3d-software (2025).
83. Thompson, A. P. et al. LAMMPS - a flexible simulation tool for particle-based materials modeling at the atomic, meso, and continuum scales. *Comp. Phys. Comm.* **271**, 108171 (2022).
84. Akiba, T., Sano, S., Yanase, T., Ohta, T. & Koyama, M. Optuna: A next-generation hyperparameter optimization framework. In *Proc. of the 25th ACM SIGK DD International Conference on Knowledge Discovery & Data Mining*. 2623–2631 (Association for Computing Machinery, New York, NY, USA, 2019).
85. Farraro, R. & Mclellan, R. B. Temperature dependence of the young's modulus and shear modulus of pure nickel, platinum, and molybdenum. *Metall. Trans. A* **8**, 1563–1565 (1977).
86. Hidnert, P. Thermal expansion of some nickel alloys. *J. Res. Natl. Bur. Stand* **58**, 89 (1957).
87. Fan, X., Case, E. D., Yang, Q. & Nicholas, J. D. Room temperature elastic properties of gadolinia-doped ceria as a function of porosity. *Ceram. Int.* **39**, 6877–6886 (2013).
88. Andersen, K. B., Charlas, B., Stamate, E. & Hansen, K. K. Permeability, strength and electrochemical studies on ceramic multilayers for solid-state electrochemical cells. *Heliyon* **3**, e00371 (2017).

Acknowledgements

The authors gratefully acknowledge funding from the German Research Foundation (DFG) for the project Ceria-based Cathodes for High Performance Electrolysis Cells (project number 467256728). The authors would like to thank the Federal Ministry of Research, Technology and Space (BMFTR) for financial support within the priority program "Mathematics for Innovations'' in the framework of “DASEA-4-SOFC”(grant number 05M2022). Additional support is provided by the Helmholtz Association, programme "Materials Science and Engineering (MSE)", no. 43.31.01, which is gratefully acknowledged. The authors acknowledge the assistance of the State of Baden-Württemberg through bwHPC. The authors would like to thank Dr. Simon Daubner for engaging in helpful discussions during this research.

Author contributions

R.K.J.: conceptualization, methodology, software, visualization, validation, writing -original draft, and writing - review and editing. A.E.: software and writing - review and editing. L.S.: software and writing - review and editing. M.W.: funding acquisition, resources, and conceptualization. A.P.: writing - review and editing. D.S.: conceptualization, project administration, and writing - review and editing. B.N.: funding acquisition, project administration, resources, supervision, and writing - review and editing.

Funding

Open Access funding enabled and organized by Projekt DEAL.

Competing interests

The authors declare no competing interests.

Additional information

Correspondence and requests for materials should be addressed to Ravi Kumar Jeela or Daniel Schneider.